JOURNAL OF PETROLOGY

Journal of Petrology, 2015, Vol. 56, No. 6, 1199–1227
doi: 10.1093/petrology/egv034
Original Article

OXFORD

The Earliest History of the Skaergaard Magma Chamber: a Textural and Geochemical Study of the Cambridge Drill Core

Marian B. Holness[1]*, Christian Tegner[2], Olivier Namur[1,3] and Llewellyn Pilbeam[1]

[1]Department of Earth Sciences, University of Cambridge, Downing Street, Cambridge CB2 3EQ, UK, [2]Department of Geoscience, Aarhus University, Høegh-Guldbergs Gade 2, DK-8000 Aarhus C, Denmark and [3]Institut fur Mineralogie, Leibniz Universität Hannover, Callinstrasse 3, 30167 Hannover, Germany

*Corresponding author. E-mail: marian@esc.cam.ac.uk

Received November 20, 2014; Accepted June 8, 2015

ABSTRACT

The Cambridge Drill Core provides a continuous sample of the lower part of the floor cumulates of the Skaergaard Intrusion, including ~150 m of stratigraphy from the unexposed Hidden Zone. Bulk-rock geochemistry together with olivine mineral compositions and augite–plagioclase–plagioclase dihedral angles from the drill core are interpreted as a record of the early history of the Skaergaard magma chamber. A detailed geochemical and microstructural study of the mode and morphology of augite reveals no unambiguous markers that can be used to pinpoint the first appearance of cumulus augite in the stratigraphy sampled by the drill core. The early history of the Skaergaard magma chamber involved the arrival of multiple small batches of magma, each with a variable load of olivine and plagioclase phenocrysts. The region of the core between –120 and –108·8 m records at least three separate, but closely spaced, influxes of new magma, with more magma added at –85 and –65 m. The last influx of magma is recorded by the cumulates just below the lowest exposed horizons of the Layered Series, involving a large volume of magma that inflated the chamber to its final size. The Skaergaard magma chamber therefore formed by the progressive inflation of what was likely to have originated as a sill intruded at the discontinuity between the Precambrian gneisses and the overlying plateau lavas. The 'Skaergaard parental magma' should therefore be viewed as the integrated and mixed composition of the various magma influxes that filled the chamber.

Key words: Skaergaard; magma chamber; intrusion; cumulate; gabbro; geochemistry; layered igneous rock; mineral chemistry

INTRODUCTION

The processes by which a magma body is emplaced in the crust are not very well understood. Field evidence points to the incremental emplacement of large bodies of silicic magma by the accumulation of many small magma batches (de Saint-Blanquat *et al.*, 2006; Michel *et al.*, 2008; Grocott *et al.*, 2009), moving predominantly along fractures (Clemens & Mawer, 1992) to form gradually inflating tabular bodies at lithological discontinuities. If the time separating each of the influxes is short, then the inflating intrusion has no time to freeze and acts as a barrier that favours the emplacement of later magma batches at the same place. Such localization of magma emplacement leads to the formation of a pluton by incremental magma addition (Annen *et al.*, 2008, 2014; Menand, 2008). Starting a magma chamber therefore is dependent on the timing between the arrival of single magma batches and the overall magma flux.

Decoding the earliest history of layered intrusions is not straightforward, and is commonly based on the study of marginal rocks (e.g. Namur *et al.*, 2011; Wilson, 2012). The Skaergaard Intrusion of East Greenland is

one of the world's best-developed examples of closed-system fractionation of basaltic magma, but little is known about the early history of the magma chamber, particularly its filling history and the composition of the incoming magma (e.g. Nielsen, 2004). Attempts to constrain the composition of the parental magma have relied on nearby dykes (e.g. Brooks & Nielsen, 1978; Nielsen, 1978) and associated flood basalts that are thought to be related to the Skaergaard, on xenoliths carried by dykes that cut the Skaergaard (Jakobsen *et al.*, 2010; Holness *et al.*, 2013*b*), on the chilled margin of the Skaergaard intrusion itself (Wager, 1960; Nielsen, 2004), and on mass summation (Nielsen, 2004; Tegner & Cawthorn, 2010). Another possible line of enquiry involves investigation of the lowermost floor cumulates, where some indications of the earliest history of the intrusion may be recorded in the cumulate stratigraphy. The base of the intrusion is not exposed but the so-called Hidden Zone was drilled in 1966 during an expedition led by Alex Deer (following the untimely death of Lawrence Wager). The resultant 350 m long Cambridge Drill Core provides ~150 m of core through the unexposed lowermost stratigraphy as well as ~200 m of the lowermost exposed stratigraphy. In this contribution we report the results of geochemical and microstructural investigations of the Cambridge Drill Core. We argue that the drill core preserves the record of multiple chamber-filling events by magmas with variable composition and crystal content. Our geochemical and microstructural data show no clear and unambiguous signature in the core that can be used to detect the stratigraphic position at which augite attains cumulus status.

THE RECORD OF MAGMA INFLUX IN LAYERED INTRUSIONS

Layered intrusions are completely solidified records of the life of a magma chamber. Their stratigraphy may record influx of new magma (e.g. Renner & Palacz, 1987; Tegner *et al.*, 1993; Eales & Cawthorn, 1996; Holness & Winpenny, 2009; Namur *et al.*, 2010) or eruption (Holness & Winpenny, 2009; VanTongeren *et al.*, 2010). Although the interpretation of this record may not be straightforward, as the cumulates formed on the margins of the magma chamber do not generally represent liquid compositions, the arrival of crystal-rich magmas may be clearly recorded by the presence of multiple, chemically distinct, disequilibrium populations of primocrysts in that part of the cumulus stratigraphy. The development of other features, such as intra-plutonic quench zones (e.g. Tegner *et al.*, 1993) or the development of resorptional features on the margins of cumulate grains, triggered by chemical disequilibrium following magma addition (e.g. Leuthold *et al.*, 2014), depends on the volumetric proportion and composition (and hence density) of the incoming magma, together with the magmastatic pressure driving the influx (e.g. Huppert & Sparks, 1980; Campbell & Turner, 1989).

If the magmastatic pressure driving the incoming magma is relatively low, an injection of dense magma will pond on the chamber floor. Because the density of basaltic magma typically increases with fractionation until saturation in Fe–Ti oxides [e.g. as suggested for the Skaergaard magma by Thy *et al.* (2009)] this means that small batches of cool, evolved magma arriving in an expanding chamber will form a gravitationally stable layer on the chamber floor (Huppert & Sparks, 1980). If the incoming magma carried a crystal load, settling of the load from such a ponded layer will create a layer of crystals at the magma–mush interface (e.g. Raedeke & McCallum, 1984). These crystals may be detectable in the final cumulates by their different chemical composition relative to the underlying layer or, if they were not in equilibrium with their carrier liquid (and they avoided complete dissolution), by resorptional features at their margins. Mixing of the new magma with that originally resident in the chamber may subsequently occur if the density difference between the two is reduced by fractionation of the two layers (Huppert & Sparks, 1980). The lower temperature of the incoming magma relative to the resident magma would mean that it would not experience undercooling and rapid crystallization, although the underlying mushy layer on the chamber floor might be chilled, perhaps resulting in relatively low clinopyroxene–plagioclase–plagioclase dihedral angles, Θ_{cpp}, in the cumulate horizon immediately underlying that marking the magma influx (e.g. Holness *et al.*, 2012*a*). The cumulates forming from the ponded layer would record a stepwise decrease in Mg-number and a decrease in forsterite content of the olivine.

If the replenishing magma is hotter and more buoyant than the resident magma, or if its ascent is driven by a high magmastatic pressure, it may not pond on the chamber floor (Campbell & Turner, 1989). If the incoming batch were significant in size relative to the volume of the resident magma we might expect to see a chill zone developed in the cumulate stratigraphy (e.g. Tegner *et al.*, 1993). Holness *et al.* (2012*a*) showed that intraplutonic quench zones are marked by a decrease in grain size and an increase in Θ_{cpp}, with the development of granular microstructures. Further characteristics of the arrival of relatively primitive magma might include the development of a layer rich in readily nucleating phases (caused by the relatively deep undercooling of the incoming magma) and an increase in Mg-number. If the incoming magma carried a significant crystal load, any layers formed by settling of this load from the mixed magma might preserve evidence of two distinct crystal populations, some of which might have resorbed margins. The development of a chill zone, resulting in the rapid crystallization of a layer of cumulates at the magma–mush interface, would form a relatively impermeable cap on the mushy layer—the cumulates below the chill zone might therefore contain high concentrations of incompatible elements owing to the higher than normal accumulation rates of crystals on the chamber floor resulting in greater volumes of

trapped interstitial liquid (Ballhaus & Glikson, 1989; Tegner *et al.*, 1993).

GEOLOGICAL SETTING

The Skaergaard Intrusion formed on the extending margin of East Greenland during the opening of the North Atlantic and was emplaced into a fault-bounded space (Irvine *et al.*, 1998; Nielsen, 2004) at the unconformity between underlying Precambrian gneisses and an overlying sequence of Tertiary volcanic rocks (Fig. 1; Wager & Deer, 1939). It is one of the world's best-known examples of extreme fractionation of basaltic magma and is generally suggested as having solidified as a closed system, with no replenishment or eruption once the chamber had reached its final size (8 km × 11 km × 4 km; Nielsen, 2004).

The intrusion is divided into three series, defined by Wager & Deer (1939): the (volumetrically dominant) Layered Series crystallized upwards from the floor; the Marginal Border Series (MBS) crystallized inwards from the (vertical or steeply dipping) walls: and the Upper Border Series (UBS) crystallized downwards from the roof. The Hidden Zone (HZ) is that part of the Layered Series that is unexposed, representing the earliest cumulates formed on the chamber floor. The Layered Series and UBS meet at the Sandwich Horizon.

Progressive fractionation within the chamber resulted in a correlated suite of changes in liquidus assemblage in each of the three series, permitting their subdivision. The exposed Layered Series is divided into Lower, Middle and Upper Zones based on the absence of cumulus olivine in the Middle Zone. The Lower Zone is further subdivided: LZa contains cumulus olivine and plagioclase; the base of LZb is marked by the arrival of cumulus augite; and the base of LZc is marked by the arrival of cumulus Fe–Ti oxides. Wager & Brown (1968) suggested that low-Ca pyroxene arrives as a cumulus phase in the upper parts of LZb, although the experimental work of Thy *et al.* (2009) suggested that oxides arrive before low-Ca pyroxene. The Upper Zone is also subdivided; the base of UZb defines the arrival of cumulus apatite, whereas the base of UZc marks the first appearance of the mosaic form of ferro-hedenbergite inverted from β-ferrobustamite. The UBS (Salmonsen & Tegner, 2013) and MBS (Hoover, 1989) can be similarly subdivided.

The thickness of each subdivision varies across the intrusion (McBirney, 1989*b*, 1996). For example, the thickness of LZa (and hence the stratigraphic height of the LZa–b boundary) varies from 175 m (McBirney, 1996; Tegner *et al.*, 2009) to 366 m (McBirney, 1989*b*).

The Cambridge Drill Core covers about 200 m of the exposed Layered Series (incorporating LZa and the lower parts of LZb), and 150 m of the HZ [the position in the core of the top of the HZ was defined using plagioclase core compositions by Maaløe (1976)]. It has been suggested, based on a consideration of the composition of plagioclase cores (Maaløe, 1976, 1978) and of augite–plagioclase–plagioclase dihedral angles (Holness *et al.*, 2007*a*), that the end of the core is close to the base of the intrusion. Published work on the Cambridge Drill Core is limited, comprising studies of pyroxenes and olivines (Nwe, 1975, 1976), plagioclase (Maaløe, 1976; Humphreys, 2009; Namur *et al.*, 2014), rhythmic layering (Maaløe, 1978, 1987) and uranium content (Henderson, 1975).

Maaløe's detailed 1976 study of plagioclase in the drill core outlines the cryptic variation and prominent variations in type of zoning with structural height. Grains with resorbed, commonly oscillatory-zoned, cores (presumed to be of primocryst origin) and generally with more albitic rims (presumed to be overgrowth from interstitial liquid) are predominant in the HZ between −150 and −100 m (Fig. 2a). Above this level they become less common with increasing stratigraphic height, disappearing entirely by 30 m stratigraphic height. Maaløe (1976) explained this disappearance as a reduction in the number of grains belonging to the population that underwent resorption, rather than to an increase in the effectiveness of the resorption. Plagioclase grains with complex and resorbed cores are generally relatively large and coexist on a thin-section scale with (generally much smaller) grains with unresorbed cores (Fig. 2a), consistent with accumulation of more than one population of plagioclase grains. Plagioclase grains with unzoned, or normally zoned, euhedral cores and more albitic rims are typical of LZa. Maaløe (1976) suggested that the grains with complex resorbed cores originated at the chamber roof, whereas those with simple euhedral cores nucleated on the chamber floor. In contrast, we will argue that the multiple populations of plagioclase provide information about the filling of the magma chamber.

Holness *et al.* (2007*a*) reported the variation of median augite–plagioclase–plagioclase dihedral angles, Θ_{cpp}, through the core. They suggested that the thermal record encoded in variations of Θ_{cpp} indicates that the chamber filled over a prolonged period, with the arrival of the last major pulse of magma recorded at the base of the exposed part of the intrusion. They noted a stepwise increase in Θ_{cpp} 100 m above the base of LZa that they attributed to the saturation of the bulk liquid in augite. Holness *et al.* (2007*b*) argued that the stepwise increase marks the top of the mush at the moment of bulk liquid augite saturation, and therefore that augite becomes cumulus at 100 m. This is some 75 m below the stratigraphic height suggested (on the basis of an increase in augite mode and a change in the field from poikilitic to granular habit) by Tegner *et al.* (2009) using a set of surface samples collected 1 km to the north of the drill core site.

Recent work has shown that dihedral angles form during the last stages of solidification, when <10 vol. % liquid remains (Holness *et al.*, 2012*a*). The dihedral angle step at 100 m in the Cambridge Drill Core therefore records a point at, or near, the base of the mushy layer on the magma chamber floor at the moment

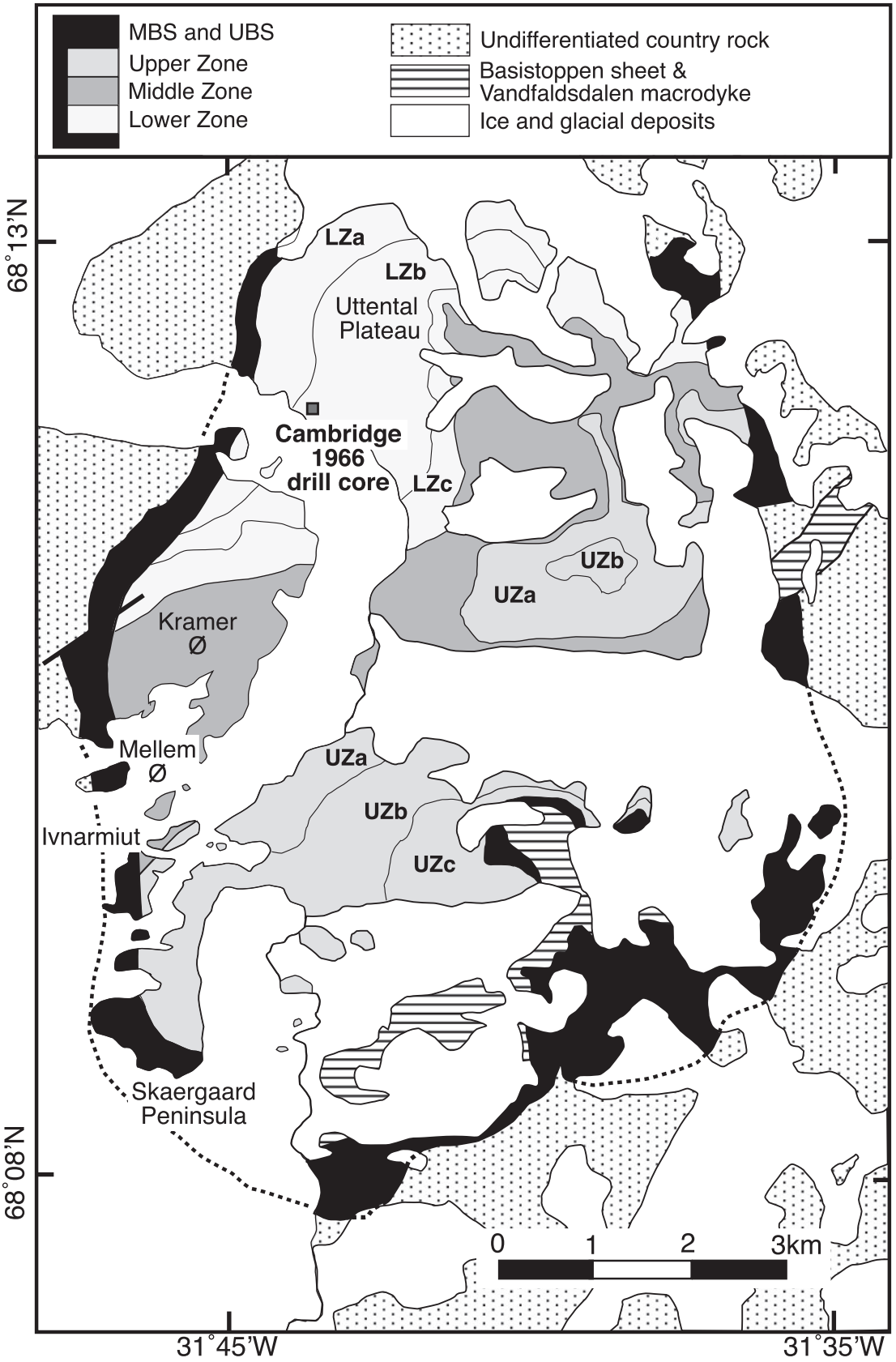

Fig. 1. Simplified geological map of the Skaergaard intrusion, after McBirney (1989*a*), showing the position of the Cambridge 1966 drill core.

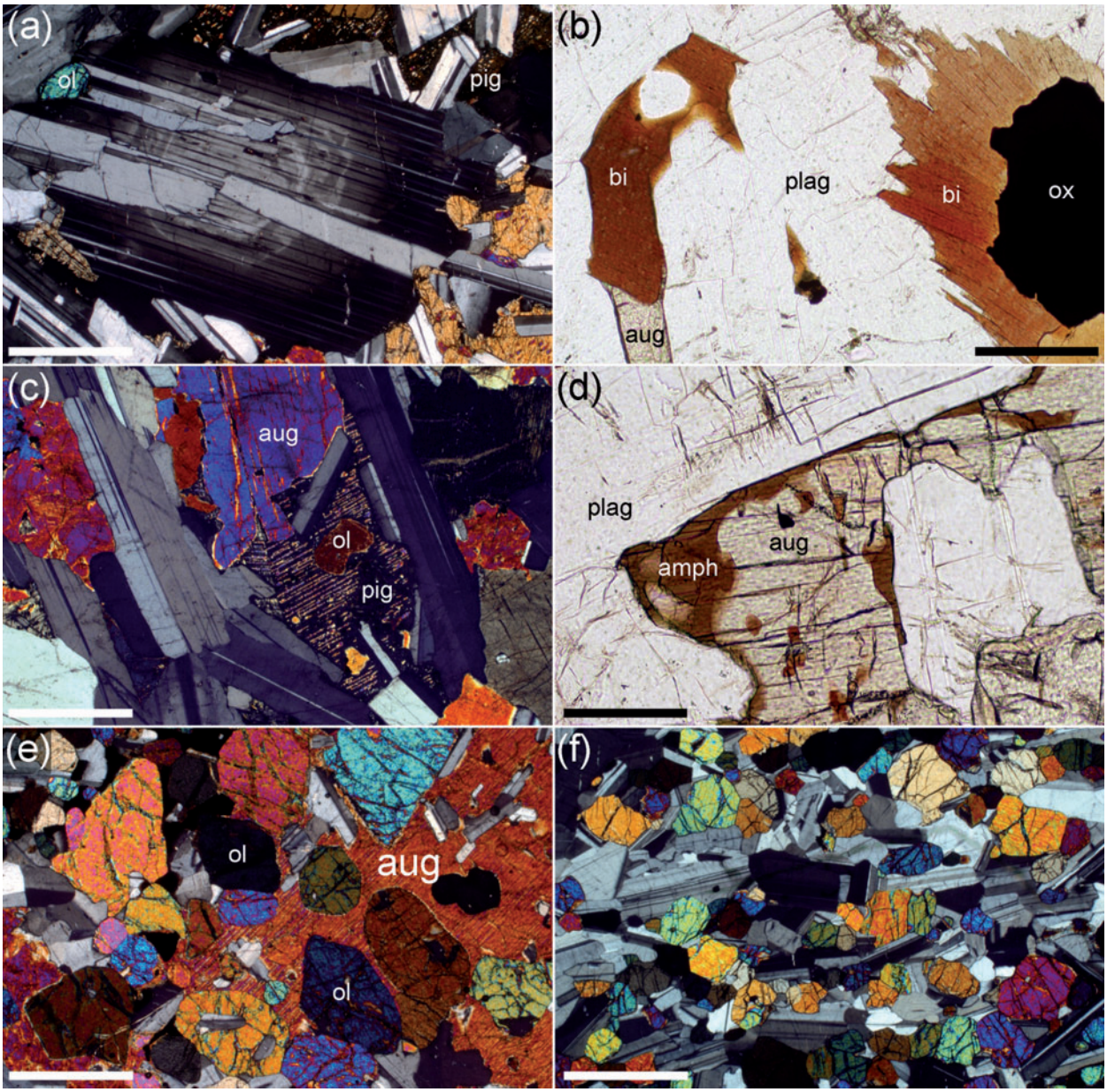

Fig. 2. Photomicrographs of thin sections of the Cambridge Drill Core. (a) A plagioclase grain with a complex, oscillatory-zoned and partially resorbed core surrounded by a more albitic rim. [Note the large size of this grain (and also its locally highly irregular twinning, perhaps indicative of grain amalgamation) in comparison with the adjacent plagioclase grains that do not have compositionally complex cores.] Sample 1060′1″ from HZ (–124·1 m stratigraphic height). (b) Biotite (bi) forms poly-crystalline rims surrounding grains of interstitial oxide (ox; right) and also (left) interstitial grains infilling spaces between cumulus plagioclase (plag). Augite grains are labelled aug. Sample 710′8″ from top of HZ (–17·6 m stratigraphic height). (c) Interstitial pyroxene can be either augite (aug) or inverted pigeonite (pig). The herringbone pattern of exsolved Ca-rich pyroxene in the grain of inverted pigeonite should be noted. Sample 153193 from the Harker Collection, University of Cambridge. (d) Interstitial augite (aug) commonly has rims of brown amphibole (amph) in a topotactic relationship. Sample 710′8″ from the top of HZ (–17·6 m stratigraphic height). (e) Olivine-rich band at –65 m stratigraphic height (sample 865′7″). The rounded olivines (ol) enclosed by augite oikocrysts should be noted. (f) Olivine-rich band at –8·8 m stratigraphic height (sample 681′1″). The average olivine grain size is much smaller in this band compared with that at –65 m and augite oikocrysts are not present. Scale bars represent 1 mm.

when the bulk magma became saturated in augite. The first appearance of cumulus augite must therefore lie somewhere above 100 m. Close sample spacing in the drill core permits us to make a detailed examination to investigate the extent to which microstructures and geochemistry can be used to constrain the first appearance of cumulus augite in the stratigraphy.

ANALYTICAL METHODS AND DATA

Bulk-rock chemistry

Bulk compositions were obtained for 121 samples from the Cambridge Drill Core, spaced ~3 m apart (Tables 1 and 2). Pieces 10–16 cm long of 1 inch diameter core were split along the long axis into pieces constituting half of the core. Using the sample preparation facilities

Table 1: Bulk compositional data (wt %) for the Cambridge drill core: major elements

Sample	Height (m)	Θ_{cpp} (°)	Θ_{cpp} (°)	Mg#	SiO_2 (%)	TiO_2 (%)	Al_2O_3 (%)	Fe_2O_3 (%)	FeO (%)	MnO (%)	MgO (%)	CaO (%)	Na_2O (%)	K_2O (%)	P_2O_5 (%)	LOI (%)	Sum (%)
13′	195·1			0·59	48·95	1·37	15·95	1·33	9·49	0·16	8·67	10·89	2·55	0·23	0·14	0·65	100·37
23′	192·0			0·56	50·68	1·53	19·56	1·51	6·34	0·12	5·44	11·44	3·15	0·29	0·10	0·55	100·72
31′ 4″	189·4	107		0·62	49·62	1·17	15·21	1·21	9·97	0·18	9·82	10·84	2·51	0·23	0·16	0·70	101·63
43′ 7″	185·7	104·5		0·60	49·21	1·89	15·73	1·30	8·82	0·16	8·41	11·84	2·53	0·21	0·14	0·66	100·90
51′ 1″	183·5			0·61	46·63	1·23	13·93	1·09	13·07	0·20	12·11	9·15	2·19	0·17	0·10	0·56	100·45
61′ 1″	180·4	103		0·59	49·21	0·84	18·53	1·02	8·59	0·15	7·72	10·49	2·83	0·25	0·23	0·58	100·42
71′ 1″	177·6	100		0·62	46·94	1·17	14·56	1·18	12·45	0·20	12·14	9·25	2·21	0·17	0·11	0·58	100·96
81′ 1″	174·3	103		0·63	50·10	1·24	16·12	1·18	7·59	0·15	8·03	12·23	2·50	0·20	0·15	0·69	100·18
92′ 11″	170·7	105		0·61	49·53	1·23	16·32	1·05	8·75	0·16	8·59	11·41	2·52	0·21	0·14	0·66	100·57
101′ 5″	168·1	99		0·60	47·56	1·23	15·04	0·96	12·47	0·20	11·13	9·63	2·28	0·15	0·06	0·59	101·31
114′ 5″	164·1			0·61	48·08	1·23	16·25	1·59	9·67	0·17	9·72	10·03	2·55	0·20	0·13	0·53	100·13
122′ 2″	161·8	100·5		0·58	49·71	1·00	20·04	1·23	7·00	0·12	6·30	10·94	3·00	0·26	0·11	0·51	100·21
132′ 3″	158·7			0·58	50·48	1·34	19·05	1·27	6·77	0·13	6·15	12·11	2·94	0·26	0·06	0·57	101·13
140′	156·3	103		0·64	45·59	0·68	9·95	1·23	16·08	0·25	16·91	7·85	1·55	0·15	0·07	0·66	100·97
153′ 11″	152·0	101	99 ± 3	0·60	49·03	1·42	17·09	1·34	9·41	0·16	8·75	10·65	2·69	0·23	0·12	0·56	101·45
161′ 11″	149·6	103		0·60	48·86	1·20	16·34	0·99	10·71	0·17	9·54	10·39	2·63	0·22	0·14	0·64	101·83
172′ 1″	146·5	102		0·59	47·75	1·70	17·28	1·36	9·25	0·15	8·43	10·58	2·68	0·23	0·09	0·52	100·01
181′ 11″	143·6	102		0·62	48·23	0·92	15·91	0·89	10·64	0·17	10·25	10·17	2·40	0·20	0·11	0·66	100·55
190′ 3″	141·0	103		0·58	49·14	1·40	19·14	0·89	7·91	0·13	6·74	11·11	2·91	0·21	0·11	0·60	100·29
201′ 11″	137·5	100		0·60	47·62	1·64	17·41	0·86	10·10	0·15	8·95	9·93	2·59	0·21	0·11	0·54	100·13
211′ 11″	134·4	101		0·61	48·33	1·15	16·42	1·08	9·65	0·16	9·32	10·67	2·54	0·20	0·13	0·56	100·21
222′ 4″	131·2	102		0·59	49·59	1·22	19·25	1·23	7·40	0·13	6·74	11·32	2·90	0·23	0·13	0·46	100·60
232′ 12″	128·0	100		0·62	47·33	1·43	15·09	1·03	11·94	0·18	11·52	9·51	2·32	0·20	0·12	0·56	101·23
242′ 1″	125·0	106·5	101 ± 2	0·59	49·57	1·24	18·68	0·94	7·98	0·14	7·07	11·28	2·86	0·23	0·14	0·55	100·67
252′ 4″	122·1	107		0·62	48·24	1·04	16·75	0·93	9·56	0·16	9·28	10·65	2·54	0·22	0·15	0·54	100·06
262′ 7″	119·0			0·61	48·17	1·05	16·18	0·60	10·52	0·17	9·51	10·39	2·54	0·20	0·13	0·57	100·03
272′ 9″	115·9	102	100 ± 2	0·62	49·32	1·20	15·50	1·49	8·75	0·16	9·26	11·73	2·40	0·20	0·11	0·53	100·68
282′ 4″	112·9	102		0·61	49·02	1·55	16·99	1·24	7·96	0·14	7·84	12·05	2·57	0·20	0·10	0·54	100·19
290′ 8″	110·4			0·59	48·90	1·37	18·20	1·57	7·90	0·14	7·59	11·10	2·78	0·21	0·09	0·57	100·42
302′ 6″	106·8	102·5		0·61	47·42	1·49	16·15	1·39	9·90	0·16	9·88	10·31	2·39	0·19	0·09	0·62	100·00
312′ 6″	103·8	99		0·60	47·45	1·78	16·71	1·39	9·61	0·16	8·94	10·38	2·57	0·21	0·10	0·65	99·95
322′ 6″	100·7	83·5		0·61	48·81	1·04	17·37	1·15	8·65	0·15	8·44	10·90	2·67	0·20	0·12	0·61	100·12
330′ 11″	98·1	81		0·61	47·66	1·24	17·25	1·04	10·09	0·16	9·43	9·96	2·57	0·20	0·10	0·54	100·25
342′ 9″	94·6	82·5		0·61	48·91	1·30	17·92	0·93	8·49	0·14	8·15	11·05	2·67	0·19	0·09	0·55	100·41
351′ 7″	91·8	82·5		0·62	48·68	0·99	17·99	1·25	8·48	0·15	8·52	10·72	2·67	0·18	0·11	0·50	100·25
361′ 5″	88·8	83		0·62	48·97	1·18	18·20	1·21	8·44	0·14	8·55	10·81	2·74	0·19	0·10	0·47	100·98
371′ 7″	85·7	82		0·61	48·09	0·99	17·75	1·31	9·21	0·15	9·18	10·19	2·60	0·20	0·12	0·45	100·22
381′ 2″	82·8	81·5	83·5 ± 2	0·59	48·44	2·33	16·67	1·63	9·46	0·17	8·84	9·77	2·49	0·23	0·11	0·57	100·72
389′ 7″	80·3	83·5		0·60	48·64	1·29	18·72	1·16	8·32	0·14	7·94	10·78	2·70	0·20	0·10	0·48	100·47
401′ 5″	76·7	83·5		0·61	48·54	1·04	18·79	1·11	8·35	0·14	8·10	10·71	2·77	0·20	0·09	0·44	100·27
411′ 5″	73·6	83·5		0·60	48·58	0·89	18·33	1·10	8·71	0·14	8·19	10·27	2·69	0·27	0·14	0·57	99·88
420′ 10″	70·7	81		0·61	48·21	1·12	17·84	0·92	9·56	0·15	9·18	10·02	2·62	0·20	0·12	0·49	100·44
430′ 6″	67·8	81		0·60	47·18	1·37	17·50	1·31	9·99	0·15	9·43	9·45	2·58	0·20	0·12	0·47	99·76
438′ 4″	65·4			0·61	46·96	1·33	17·34	1·56	10·20	0·16	10·17	9·30	2·58	0·20	0·11	0·43	100·35
450′ 11″	61·0	81·5		0·61	48·00	1·00	17·92	1·12	9·72	0·16	9·34	9·83	2·65	0·20	0·13	0·50	100·58
460′ 11″	58·5	82		0·60	47·81	1·36	17·53	1·33	9·54	0·16	9·03	9·88	2·61	0·22	0·15	0·49	100·12
470′ 11″	55·5	80·5		0·61	47·94	1·10	18·32	0·63	9·61	0·15	8·67	10·02	2·71	0·22	0·12	0·54	100·03
481′ 1″	52·4	81·5		0·62	47·16	1·28	16·59	1·29	10·74	0·17	10·69	9·34	2·51	0·20	0·11	0·51	100·60
490′ 11″	49·4	84		0·62	48·25	1·29	17·28	0·73	9·72	0·16	9·36	10·23	2·55	0·23	0·14	0·59	100·53
499′ 2″	46·9			0·63	46·54	1·07	15·55	1·40	11·57	0·18	12·29	8·67	2·33	0·20	0·13	0·55	100·47
511′ 1″	43·2			0·63	47·50	0·96	16·18	0·99	11·31	0·18	11·31	9·22	2·40	0·20	0·13	0·55	100·93
522′ 1″	39·9	77·5		0·62	47·78	1·24	15·94	1·23	10·69	0·18	10·74	10·18	2·30	0·19	0·08	0·59	101·14
531′ 7″	37·0			0·60	48·22	1·04	19·41	0·71	8·87	0·14	8·04	10·89	2·61	0·17	0·10	0·61	100·81
539′ 11″	34·4	78	81 ± 3	0·57	49·34	1·08	21·74	1·44	6·36	0·11	5·63	11·45	2·88	0·19	0·10	0·43	100·75
551′ 7″	30·9			0·58	49·53	0·81	21·63	0·93	6·96	0·12	6·05	11·41	2·93	0·19	0·14	0·51	101·20
561′ 1″	28·0	78	80 ± 4	0·59	49·28	0·96	21·18	1·28	6·77	0·11	6·34	11·32	2·87	0·22	0·12	0·50	100·96
571′ 4″	24·8	80·5	80 ± 2	0·57	49·71	0·94	22·47	0·88	6·11	0·10	5·06	11·70	3·03	0·22	0·14	0·50	100·87
581′ 1″	21·9	83·5	84 ± 2	0·59	49·66	1·03	21·86	0·94	6·27	0·11	5·66	11·74	2·87	0·20	0·09	0·54	100·97
588′ 1″	19·8		84·5 ± 2	0·60	48·81	0·89	20·81	1·33	7·20	0·12	7·02	11·05	2·77	0·19	0·10	0·53	100·83
601′ 1″	15·8	86	86·5 ± 2	0·58	49·62	1·12	22·45	1·01	6·26	0·10	5·50	11·67	2·96	0·19	0·09	0·41	101·37
611′ 1″	12·7	84	86 ± 2·5	0·60	49·07	0·75	21·79	0·80	6·97	0·11	6·44	11·17	2·91	0·18	0·10	0·42	100·70
621′ 2″	9·7	92	93 ± 2	0·63	49·39	0·79	20·64	0·56	6·94	0·12	6·94	11·90	2·69	0·17	0·08	0·46	100·68
631′ 1″	6·6	91·5	91·5 ± 2·5	0·60	48·73	0·93	21·89	0·96	6·89	0·11	6·52	11·08	2·83	0·18	0·10	0·41	100·62
639′ 3″	4·2		91 ± 3	0·61	49·33	0·86	21·67	0·94	6·64	0·11	6·59	11·40	2·84	0·18	0·08	0·42	101·07
651′ 2″	0·5	91	93·5 ± 2·5	0·62	48·92	0·95	21·41	0·90	6·71	0·11	6·78	11·51	2·82	0·17	0·08	0·46	100·80
661′ 7″	–2·5	93	96 ± 1·5	0·64	48·68	0·87	20·95	0·84	7·31	0·12	7·82	11·05	2·70	0·15	0·07	0·50	101·07
671′ 1″	–5·5	85·5	86 ± 2	0·68	47·38	0·48	19·49	0·84	8·18	0·14	10·64	10·10	2·46	0·13	0·04	0·54	100·41
681′ 1″	–8·6	85·5	86 ± 1·5	0·69	46·01	0·30	16·98	0·89	10·67	0·17	14·07	8·85	2·12	0·10	0·04	0·43	100·62
681′ 7″	–8·8	85·5		0·67	44·45	0·54	13·53	0·68	13·28	0·19	15·48	8·27	1·73	0·09	0·06	0·53	98·83

(continued)

Table 1: Continued

Sample	Height (m)	Θ_{cpp} (°)	Θ_{cpp} (°)	Mg#	SiO_2 (%)	TiO_2 (%)	Al_2O_3 (%)	Fe_2O_3 (%)	FeO (%)	MnO (%)	MgO (%)	CaO (%)	Na_2O (%)	K_2O (%)	P_2O_5 (%)	LOI (%)	Sum (%)
690′ 11″	–11·6	84·5		0·63	47·93	0·92	18·57	1·14	8·70	0·15	9·26	10·40	2·58	0·20	0·12	0·55	100·52
700′ 8″	–14·6	81·5	85 ± 2	0·60	48·06	1·38	19·23	1·18	8·50	0·15	7·97	10·46	2·68	0·23	0·12	0·50	100·46
710′ 8″	–17·6	79·5	85 ± 1·5	0·63	46·70	1·29	16·32	1·03	11·18	0·19	11·44	9·08	2·31	0·21	0·10	0·50	100·35
722′ 8″	–20·6	83·5	86 ± 2	0·62	48·50	0·92	20·30	0·94	7·71	0·13	7·64	9·77	3·00	0·36	0·26	0·57	100·09
730′ 9″	–23·7			0·60	48·28	1·33	20·52	1·26	7·64	0·13	7·18	10·14	2·97	0·29	0·18	0·44	100·37
738′ 9″	–27·3	84·5	86·5 ± 2	0·64	47·33	1·08	16·16	1·15	10·16	0·18	11·26	10·20	2·22	0·18	0·08	0·50	100·50
750′ 5″	–29·7			0·63	48·72	0·85	19·84	0·73	7·40	0·13	7·69	11·45	2·68	0·21	0·09	0·48	100·28
760′ 7″	–31·6	82·5		0·60	48·52	1·10	20·50	0·73	7·60	0·13	6·91	11·13	2·74	0·23	0·09	0·52	100·19
770′ 5″	–35·8	81		0·61	47·79	1·10	19·68	0·78	8·91	0·15	8·45	9·98	2·64	0·21	0·13	0·52	100·34
780′ 5″	–38·8	83·5		0·64	47·65	0·83	18·75	0·85	8·34	0·14	8·99	10·45	2·61	0·23	0·12	1·35	100·31
792′ 5″	–41·3	82		0·63	47·10	1·24	18·24	0·94	9·92	0·16	10·17	9·35	2·52	0·24	0·14	0·50	100·54
800′ 5″	–45·0	85		0·61	48·00	1·02	19·91	0·77	9·06	0·15	8·59	9·88	2·68	0·22	0·09	0·47	100·84
818′ 5″	–50·5	86		0·62	47·91	1·04	20·43	0·71	8·37	0·14	8·07	10·27	2·71	0·22	0·16	0·50	100·52
829′ 11″	–56·4	82		0·63	47·82	1·09	19·25	0·43	9·02	0·14	9·06	10·67	2·51	0·20	0·10	0·50	100·80
842′ 3″	–57·7	81	84 ± 3	0·63	47·60	1·11	18·91	0·94	9·37	0·16	9·78	9·69	2·46	0·20	0·13	0·48	100·83
849′ 10″	–60·0	83		0·64	46·88	1·12	17·58	0·99	10·24	0·17	11·14	9·60	2·31	0·19	0·12	0·47	100·81
854′ 4″	–61·4			0·63	48·07	1·01	20·13	0·97	8·09	0·13	8·45	10·50	2·59	0·19	0·13	0·49	100·76
862′ 1″	–63·2	85·5		0·65	47·26	0·93	18·42	0·63	9·84	0·16	10·67	9·85	2·33	0·18	0·07	0·45	100·79
864′ 1″	–64·4			0·68	42·62	0·77	8·64	1·45	17·57	0·26	22·73	5·65	1·15	0·07	0·05	0·60	101·55
867′ 3″	–66·2	89·5	86 ± 2	0·69	42·19	1·04	7·80	1·00	17·95	0·28	23·42	5·18	1·11	0·14	0·13	0·68	100·92
879′ 12″	–69·2	88		0·65	48·25	0·91	19·58	0·70	8·39	0·14	9·45	10·28	2·58	0·20	0·09	0·44	101·02
887′ 10″	–73·6	88·5		0·63	47·15	1·25	19·30	0·00	10·22	0·15	9·50	9·69	2·61	0·21	0·13	0·58	100·78
900′ 1″	–75·3	87		0·64	46·93	1·08	17·40	0·77	10·53	0·18	10·99	9·81	2·24	0·16	0·09	0·46	100·62
911″	–78·3	86		0·63	49·04	0·98	20·29	0·44	7·28	0·13	7·25	11·95	2·63	0·20	0·07	0·47	100·73
920′ 2″	–81·5	85·5		0·61	47·91	1·59	19·67	0·59	8·76	0·15	7·93	10·73	2·53	0·20	0·07	0·47	100·60
930′ 2″	–84·5	82		0·60	49·37	1·00	21·28	0·11	8·45	0·14	7·13	10·61	2·80	0·24	0·16	–0·44	100·84
933′	–85·4			0·60	48·36	1·25	20·29	0·92	8·47	0·13	7·62	10·43	2·59	0·22	0·13	0·49	100·92
937′ 1″	–86·6			0·65	46·12	0·79	17·05	1·38	10·54	0·17	12·37	9·43	2·04	0·13	0·08	0·85	100·95
940′ 6″	–88·7	81	83·5 ± 3	0·66	47·31	0·66	18·07	0·04	10·43	0·16	11·13	10·25	2·22	0·15	0·05	0·61	101·09
949′ 11″	–90·5	86·5		0·65	48·13	0·81	20·40	0·31	8·32	0·13	9·02	10·13	2·70	0·21	0·14	0·57	100·88
959′ 11″	–93·6	85		0·65	48·63	0·87	20·69	0·57	7·55	0·13	8·38	10·70	2·66	0·21	0·09	0·51	101·00
979′ 11″	–99·7	82·5		0·66	46·54	0·86	16·25	1·05	10·89	0·18	12·83	9·31	2·10	0·16	0·10	0·55	100·83
991′ 9″	–103·3	84·5		0·66	48·48	0·79	18·73	0·93	7·94	0·15	9·31	11·13	2·45	0·19	0·08	0·56	100·73
999′ 11″	–105·8	82·5		0·64	47·64	1·23	17·65	0·58	10·14	0·17	10·65	9·78	2·30	0·19	0·06	0·61	101·01
1009′ 10″	–108·8	88		0·65	47·81	0·87	17·01	0·89	9·70	0·17	10·77	10·68	2·23	0·17	0·06	0·59	100·95
1019′ 11″	–111·9	93		0·60	48·92	0·74	19·30	0·77	8·21	0·15	7·49	11·38	2·60	0·22	0·12	0·47	100·37
1029′ 11″	–114·9	90		0·63	49·33	1·12	19·13	0·40	7·52	0·14	7·39	12·32	2·52	0·19	0·06	0·52	100·65
1037′ 10″	–117·3	95·5	96·5 ± 3	0·58	48·32	1·88	19·22	1·01	8·47	0·15	7·31	11·17	2·61	0·21	0·08	0·44	100·87
1049′ 11″	–121·0	84·5	83 ± 3·5	0·57	49·04	1·15	19·26	0·59	8·99	0·16	7·09	10·84	2·68	0·25	0·17	0·67	100·90
1060′ 1″	–124·1	78		0·56	47·57	1·14	18·22	0·29	11·76	0·18	8·38	9·07	2·63	0·29	0·17	0·73	100·43
1070′ 2″	–127·2	72·5	77 ± 3·5	0·59	48·63	1·09	19·90	0·91	8·21	0·15	7·10	10·99	2·68	0·24	0·12	0·60	100·63
1079′ 11″	–130·8	80		0·60	47·88	1·10	18·35	0·78	9·91	0·17	8·92	10·12	2·52	0·22	0·10	0·54	100·61
1091′ 6″	–133·7	76·5	79 ± 3·5	0·61	49·70	0·93	20·35	1·43	5·60	0·12	5·92	12·60	2·71	0·23	0·06	0·91	100·58
1101′ 5″	–136·7			0·57	48·22	1·55	19·62	1·46	7·57	0·15	6·54	11·29	2·61	0·24	0·11	1·26	100·64
1108′	–138·7			0·59	47·60	1·22	19·20	1·22	7·50	0·15	6·90	11·36	2·40	0·23	0·12	2·54	100·45
1112′ 3″	–141·0	78		0·60	48·98	0·88	19·60	1·61	6·52	0·14	6·69	11·92	2·58	0·21	0·09	1·39	100·61
1117′ 8″	–141·7	77·5		0·60	48·56	0·95	18·88	1·98	6·73	0·14	7·15	11·94	2·43	0·18	0·06	1·46	100·46
1122′ 3″	–143·1			0·61	48·83	1·07	18·67	1·30	7·52	0·14	7·49	11·73	2·45	0·21	0·09	1·17	100·68
1144′	–149·7			0·59	48·99	1·07	19·45	2·08	5·82	0·13	6·26	12·45	2·55	0·18	0·11	1·41	100·51
1145′ 3″	–150·0	75·5		0·57	48·64	1·43	20·21	1·48	6·45	0·14	5·65	11·42	2·84	0·34	0·10	1·94	100·63

The sample number refers to depth in core, measured in feet and inches. The values for Θ_{cpp} shown in the third column are taken from Holness *et al.* (2007a,b) and were not presented with estimates of uncertainties; those in the fourth are from the present study. Mg-number is calculated using FeO_{tot}. LOI, loss on ignition.

at Aarhus University, each sample was crushed into <2 cm sized aggregate in a hydraulic (steel) piston press and split into two portions, each of 30–40 g. The corundum shatterbox was pre-contaminated by pulverizing an aliquot for 3–5 min. This aliquot was then removed and the shatterbox was cleaned in ethanol before the second aliquot was pulverized to a fine powder for geochemical analysis.

The mass lost on ignition was determined by heating the powder in air in a muffle furnace at 950°C for 3 h. Fused glasses were prepared by mixing 0·75 g ignited sample with 3·75 g of Fluore-X65 HP (a commercial flux from Socachim Fine Chemicals consisting of 66 wt % $Li_2B_4O_7$ and 34 wt % $LiBO_2$) in a 30 ml 95Pt–5Au crucible. The crucible was transferred to a muffle furnace and the contents were melted twice for 5 min at 1150°C, with swirling of the crucible between melting. After fusion, the melt was poured into a red-hot, 32 mm 95Pt–5Au mould and quenched in air to a flat glass disc that was used for analysis of major elements. Powder pellets were prepared by thoroughly mixing 6·0 g sample powder with 1·0 g phenol formaldehyde (British Bakelite Company; resin R0214). After mixing, the powder was placed in an X-ray die and pressed in a hydraulic press

Table 2: Bulk compositional data (ppm) for the Cambridge drill core: trace elements

Sample	Height (m)	Ba	V	Cr	Ni	Cu	Zn	Sr	Y	Zr
13′	195·1	62	214	182	170	98	78	258	19	88
23′	192	73	220	161	96	95	61	321	21	90
31′ 4″	189·4	62	236	205	184	107	79	243	20	85
43′ 7″	185·7	56	297	254	149	113	73	255	20	78
51′ 1″	183·5	51	203	139	266	157	174	225	13	56
61′ 1″	180·4	59	174	115	165	125	71	300	21	66
71′ 1″	177·6	53	198	125	275	110	98	235	15	59
81′ 1″	174·3	51	293	219	125	76	67	256	22	76
92′ 11″	170·66	54	238	176	156	85	74	265	19	72
101′ 5″	168·1	37	180	129	246	76	100	245	12	42
114′ 5″	164·1	63	213	123	209	93	83	263	18	71
122′ 2″	161·8	61	153	83	127	99	64	324	20	78
132′ 3″	158·7	52	243	186	103	91	65	301	22	81
140′	156·3	45	175	188	457	135	125	155	15	59
153′ 11″	152	58	219	155	183	117	82	268	19	77
161′ 11″	149·6	68	202	133	207	145	84	264	18	66
172′ 1″	146·5	58	220	147	183	109	74	280	16	78
181′ 11″	143·6	49	172	145	218	105	86	258	16	59
190′ 3″	141	56	180	118	136	102	65	307	18	78
201′ 11″	137·5	57	205	101	203	115	75	287	16	76
211′ 11″	134·4	52	197	169	199	121	78	264	17	60
222′ 4″	131·2	65	179	140	140	113	65	309	17	70
232′ 12″	128	49	206	140	265	118	92	244	16	78
242′ 1″	125	43	181	148	140	112	69	304	19	69
252′ 4″	122·1	51	191	143	195	112	77	270	19	61
262′ 7″	119	46	187	147	207	133	80	266	17	56
272′ 9″	115·9	54	250	279	177	113	75	250	19	72
282′ 4″	112·9	50	252	251	152	105	68	273	17	68
290′ 8″	110·4	49	218	155	156	103	70	294	16	69
302′ 6″	106·8	62	228	152	223	98	81	258	16	71
312′ 6″	103·75	54	226	166	202	112	80	272	16	77
322′ 6″	100·7	47	192	163	179	101	71	280	17	63
330′ 11″	98·14	48	173	120	218	126	80	277	15	70
342′ 9″	94·6	50	196	140	171	96	68	287	15	60
351′ 7″	91·8	40	152	134	188	95	72	292	15	49
361′ 5″	88·8	50	180	150	202	93	74	293	16	62
371′ 7″	85·7	45	158	130	218	102	75	284	16	60
381′ 2″	82·8	68	279	101	174	132	84	267	20	116
389′ 7″	80·3	51	177	115	179	98	69	294	16	64
401′ 5″	76·65	45	157	100	191	93	69	301	16	54
411′ 5″	73·6	54	147	85	189	110	74	289	22	112
420′ 10″	70·7	48	158	73	216	108	75	300	16	67
430′ 6″	67·8	53	176	58	235	121	80	281	16	73
438′ 4″	65·4	48	164	58	257	123	84	279	14	67
450′ 11″	61	52	140	71	231	102	79	294	16	67
460′ 11″	58·5	58	183	83	214	110	81	285	18	87
470′ 11″	55·5	52	148	71	208	117	76	294	16	71
481′ 1″	52·4	54	180	45	263	112	88	269	16	67
490′ 11″	49·37	55	188	123	232	114	74	278	18	77
499′ 2″	46·86	60	159	64	314	100	89	250	17	65
511′ 1″	43·2	48	148	81	285	108	92	259	16	63
522′ 1″	39·9	54	201	120	253	97	88	259	17	72
531′ 7″	36·98	42	143	80	188	75	75	305	15	52
539′ 11″	34·44	48	129	54	127	88	59	343	16	55
551′ 7″	30·9	38	125	65	142	100	61	328	16	48
561′ 1″	28	47	140	72	148	91	62	331	17	60
571′ 4″	24·8	51	128	71	115	88	55	344	19	70
581′ 1″	21·9	51	138	58	123	85	56	338	17	55
588′ 1″	19·76	42	118	71	166	98	66	310	15	49
601′ 1″	15·8	44	142	69	126	88	58	339	15	62
611′ 1″	12·7	37	107	55	156	85	58	335	14	35
621′ 2″	9·7	38	135	119	146	61	59	315	16	46
631′ 1″	6·6	47	109	53	168	74	58	338	13	46
639′ 3″	4·16	34	114	64	162	75	59	330	14	49
651′ 2″	0·5	39	123	99	162	71	56	329	13	47
661′ 7″	–2·5	23	112	75	210	67	63	322	12	40
671′ 1″	–5·5	26	82	69	247	45	58	297	8	21
681′ 1″	–8·6	8	59	67	396	32	75	256	7	17
681′ 7″	–8·7	27	120	125	443	47	99	207	10	25
690′ 11″	–11·6	38	140	73	224	95	71	296	15	54
700′ 8″	–14·6	57	173	44	187	115	71	304	17	74
710′ 8″	–17·6	46	170	49	296	125	89	259	13	69
722′ 8″	–21·3	72	114	11	198	139	63	325	21	110
730′ 9″	–23·7	55	151	18	190	136	64	325	18	104
738′ 9″	–26·2	39	172	113	268	88	79	256	15	55
750′ 5″	–29·7	50	147	87	169	78	59	309	16	50
760′ 7″	–32·8	48	154	43	163	87	63	317	15	71
770′ 5″	–35·8	43	139	24	211	116	70	308	14	66
780′ 5″	–38·9	53	140	70	224	82	68	295	15	62
792′ 5″	–42·5	62	149	24	278	112	81	289	15	81
800′ 5″	–45	38	120	17	224	107	72	309	13	67
818′ 5″	–50·5	45	129	15	214	117	68	312	14	67
829′ 11″	–53·9	39	159	58	230	85	69	288	14	61
842′ 3″	–57·7	40	140	20	265	122	77	289	15	64
849′ 10″	–60	41	148	55	305	102	79	270	13	68
854′ 4″	–61·4	32	124	58	241	89	67	311	15	60
862′ 1″	–63·8	38	131	55	290	85	75	279	11	51
864′ 1″	–64·37	23	126	78	725	68	135	141	8	27
867′ 3″	–65·3	33	136	48	758	117	134	129	12	61
879′ 12″	–69·2	37	123	46	246	89	64	304	13	55
887′ 10″	–71·6	40	130	25	248	110	73	305	15	80
900′ 1″	–75·3	35	151	59	281	111	79	267	12	50
911″	–78·7	44	164	88	156	67	56	310	15	49
920′ 2″	–81·5	42	192	32	191	98	68	303	13	63
930′ 2″	–84·5	36	111	76	285	63	71	275	11	36
933′	–85·37	50	142	46	215	123	73	311	17	81
937′ 1″	–86·62	28	114	65	383	83	83	261	11	46
940′ 6″	–87·7	51	120	10	158	101	63	329	16	68
949′ 11″	–90·5	42	103	19	225	90	62	323	14	60
959′ 11″	–93·6	32	117	32	196	73	54	319	14	51
979′ 11″	–99·7	36	139	56	361	86	85	250	13	56
991′ 9″	–103·3	47	148	103	222	77	63	290	15	49
999′ 11″	–105·8	42	167	44	267	84	75	273	13	52
1009′ 10″	–108·8	35	167	98	263	74	76	261	13	41
1019′ 11″	–111·9	53	151	58	172	111	70	305	16	66
1029′ 11″	–114·9	40	211	115	148	73	59	293	14	45
1037′ 10″	–117·3	55	210	65	164	102	70	298	14	69
1049′ 11″	–121	57	153	95	144	114	72	311	19	83
1060′ 1″	–124·1	67	135	11	214	169	93	299	19	105
1070′ 2″	–127·2	43	156	73	154	120	70	306	15	68
1079′ 11″	–130·2	46	157	62	216	102	79	288	15	67
1091′ 6″	–133·7	48	180	99	118	73	54	314	15	55
1101′ 5″	–136·7	61	226	45	144	106	69	321	16	80
1108′	–138·7	50	201	58	174	101	64	280	15	69
1112′ 3″	–140	51	173	71	151	82	61	303	15	55
1117′ 8″	–141·7	37	200	62	164	69	62	287	14	44
1122′ 3″	–143·1	43	191	68	159	84	62	287	15	54
1144′	–149·7	48	215	108	127	97	59	296	16	63
1145′ 3″	–150·1	64	204	46	121	114	58	329	16	82

The sample number refers to depth in core, measured in feet and inches.

for 5 min at 30 tons. The pellet was dried at 110°C for 30 min until the phenol formaldehyde was set.

Major and the trace element compositions were analysed on a PANalytical PW2400 X-ray spectrometer using SuperQ software at Aarhus University. For the major elements we used a 3 kW Rh tube, operating at 50 kV and 55 mA using a PX-1 multilayer crystal for Na and Mg, a PE crystal for Al and Si, a Ge crystal for P, a LiF(200) crystal for K, Ca and Ti, and a LiF(220) crystal for Mn and Fe. The detector was a gas flow proportional counter using P10 (10% methane in Ar) gas. For Mn and Fe, this detector was used in tandem with a sealed Xe

detector. FeO was determined by titration using potassium dichromate. The trace elements Ba, V and Cr were analysed on a Rh tube operated at 50 kV and 55 mA. The trace elements Ni, Cu, Zn, Sr, Y and Zr were analysed using a Rh tube operated at 60 kV and 45 mA. A LiF(200) crystal and 100 μm collimator were used throughout. Ba, V and Cr were detected in a gas flow proportional counter using a sealed Xe counter in tandem for V and Cr.

A set of 44 international silicate rock reference materials, with compositions ranging from basalt to rhyolite, was used for the calibrations (Govindaraju, 1994, 1995). For the major elements matrix corrections were made using the fundamental parameter (FP) model (van Sprang, 2000; Thomsen, 2007). For Ni, Cu, Zn, Sr, Y and Zr the mass attenuation corrections are based on measuring the intensity of the Compton Kα line of Rh. For Ba, V and Cr, the FP matrix correction model was used. The samples were analysed in two sessions together with two internal house standards ($n = 11$) showing offsets between the two datasets of 10% and 22% for Zr and Y, respectively; these elements have been adjusted accordingly in the data reported in Tables 1 and 2. Supplementary Dataset 1 shows that measured values for standard BHVO-1 ($n = 4$) are reproduced with a relative standard deviation of less than 3% for all elements (except Ba < 7%) and within 8% of the certified values (supplementary data are available for downloading at http://www.petrology.oxfordjournals.org).

Mineral compositions

Mineral compositions were analysed at both Aarhus and Cambridge universities. The Aarhus analyses include all reported plagioclase compositions, major element compositions of Ca-rich pyroxene, and some olivine analyses. Mineral compositions were determined with a JEOL JXA-8600 electron microprobe, using a combination of wavelength-dispersive (WDS) and energy-dispersive (EDS) methods. Analyses were carried out using a 20 kV acceleration voltage, 10 nA beam current and an ~2 μm beam width, using synthetic and natural standards for element calibration and ZAF correction procedures. For olivine and clinopyroxene EDS (120 s) was used for Mg, Si and Fe, and WDS for Mn and Ni (40 s). For plagioclase EDS (200 s) was used for Na, Al, Si and Ca, and WDS (40 s) for K and Fe. Plagioclase was analysed using a defocused electron beam with a diameter of 10 μm to minimize the effect of Na and K volatilization. Olivine and clinopyroxene were analysed using a slightly defocused electron beam with a diameter of 2 μm. Mineral compositions were commonly characterized by a total of 6–9 spot analyses from the cores of at least three crystals within each sample.

Olivine and clinopyroxene compositions analysed at Cambridge were obtained with a Cameca SX-100 electron microprobe. A 15 kV and 10 nA focused beam was used with a spot size of 1 μm. Peak counting times were 20 s for major elements and 40 s for minor elements. When possible, at least three points in the cores of three grains ($n > 9$) were measured. The following standards were used for Kα X-ray lines calibration: diopside for Si and Ca; rutile for Ti; corundum for Al; spessartine for Mn; fayalite for Fe; periclase for Mg; jadeite for Na; K-feldspar for K; NiO for Ni; Cr for Cr. Crystals used in spectrometers were TAP for Si, Ti, Al and Mg; PET for Ca, Na and K; and LIF for Mn, Fe, Cr and Ni. Raw data were corrected with the CITZAF software (Armstrong, 1995). The full set of mineral analyses obtained using the electron microprobe are given in Supplementary Datasets 2 (olivine), 3 (clinopyroxene) and 4 (plagioclase).

In situ mineral trace element analyses of clinopyroxene were performed using laser ablation inductively coupled plasma mass spectrometry (LA-ICP-MS) at the University of Cambridge. A pulsed 213 nm New Wave Research UP213 Nd:YAG laser with 100 mJ energy at a repetition rate of 10 Hz coupled with an Elan DCR II quadrupole ICP-MS system was used for ablation. Laser sampling was performed in a He–Ar atmosphere with a beam diameter of 100 μm. Analyses were calibrated using ^{57}Ca and ^{29}Si as internal standard isotopes based on CaO and SiO_2 concentrations measured by electron microprobe. During time-resolved analyses of minerals, possible contamination from inclusions and fractures was detected by monitoring several elements and only the 'clean' part of the signals was integrated. NIST glasses (610 and 612; Pearce *et al.*, 1997) were used as external standards, and NIST-614, BCR-2G, BIR-1G, GOR-128-G (Horn *et al.*, 1997; Norman *et al.*, 1998; Jochum *et al.*, 2005, 2006) and in-house standards were used as secondary standards. The reproducibility of trace element results for the BCR glasses using the Cambridge analytical protocols is between 0·5 and 4% relative (1σ) for the majority of elements. Data were reduced using Glitter 4.0 (Griffin *et al.*, 2008). The analyses are presented in Supplementary Dataset 5.

Mineral modes

Mineral modes were determined for a selection of samples through the drill core using image analysis of high-resolution scans of entire standard-sized thin sections, combining direct analysis of scans with analysis of hand-drawn overlays. Given the absence of strong grain fabrics in the drill core we assumed that the areal extent of each phase in a thin section is representative of its volumetric proportion. We chose samples with relatively small grain size and compositional homogeneity (on the thin-section scale). The volume proportions of oxides (undifferentiated) and plagioclase were determined directly using ImageJ (Rasband, 2007) on a thresholded scanned image. The areal extent of olivine was determined by outlining all olivine grains and then flooding the outlines to create a black and white image. The volume proportion of low-Ca pyroxene (inverted pigeonite) was determined by drawing around each Ca-poor pyroxene grain on an overlay, checking each grain using a microscope. The proportion of augite in a

randomly chosen subset of the samples was calculated by point counting 1000 points per section, with comparison made between these values and calculation by difference (ignoring the small amounts of biotite and apatite). The values obtained by these two methods are similar. The results are shown in Table 3 [together with data from Nwe (1975)], with the stratigraphic position of each analysed sample shown in Fig. 3.

We measured the mineral modes in the LZa samples from the sample suite described by Tegner *et al.* (2009) to ensure comparability with our drill core data. The results are shown in Table 4

Grain size and shape

There are inherent errors associated with microstructural quantification using thin sections: the most significant is because thin sections necessarily comprise two-dimensional (2-D) sections through a three-dimensional (3-D) texture. This cut will rarely intersect the centre of the object, and small objects are less likely to be cut. Statistical techniques can be used to quantify the effect of this random sectioning on grain-size distributions [a thorough review has been presented by Royet (1991)], although some of these methods rely on the assumption that all grains have the same shape (e.g. Higgins, 2000) and this is unlikely to be true for intercumulus grains or oikocrysts. A similar difficulty arises for quantification of 3-D grain shape: existing methods are based on the assumption that all grains in a sample have the same shape (e.g. Higgins, 1994) and, again, this is unlikely to be the case for intercumulus and poikilitic grains. We made no attempt to convert our 2-D measurements into 3-D data. Other errors in textural quantification are associated with minor inaccuracies in the tracing and in the measurement of the area of the thin section (of the order of ± 10 mm^2).

Olivine grain size was determined by averaging the long dimension of all grains visible in one particular area of each thin section (up to 50 grains per sample), with no stereological corrections.

Clinopyroxene morphology was quantified for a subset of 30 samples, chosen to cover the length of the core, with a relatively close spacing in the region of 100 and 175 m (see Fig. 3 for the stratigraphic positions of analysed samples). Whereas clinopyroxene at the top of the drill core forms compact equant grains, it is generally poikilitic in the lower parts. The oikocrysts contain abundant large plagioclase grains, and the volume proportion of clinopyroxene in each oikocryst is generally similar to, or lower than, that of the enclosed plagioclase. This means that each oikocryst, as observed in thin section, comprises a group of patches of clinopyroxene, all in optical continuity, that are entirely separated from each other (in the plane of the thin section) by plagioclase. Their continuity in three dimensions, out of the plane of the section, is shown by them being in optical continuity. We term each of these patches a domain.

The edges of each augite grain or domain were outlined by hand on high-resolution images, using an optical microscope to check the drawings (Fig. 4). In those samples containing oikocrysts, each optically distinct group of domains was assigned a different grey-scale fill. For each thin section a separate image was created in which single oikocrysts were outlined by polygons, each drawn by eye (i.e. the polygon encloses all clinopyroxene domains that form a group in optical continuity; Fig. 4). Images were analysed using ImageJ to obtain the area and position of each domain, the area enclosed by the polygons (taken to be the area of the entire oikocryst), and the total volumetric proportion of augite. We also determined the number of domains in each oikocryst that were intersected by the plane of the thin section.

Dihedral angles

The median clinopyroxene–plagioclase–plagioclase dihedral angle, Θ_{cpp}, was determined using a universal stage mounted on an optical microscope with a Leitz UM32 objective. For each sample we measured 50–100 three-grain junctions. The number of measurements was chosen to reduce the 95% confidence interval [determined according to the method of Stickels & Hücke (1964)] below $\pm 3{\cdot}5^\circ$. The medians and the 95% confidence intervals are reported in Table 1, together with the previously published data of Holness *et al.* (2007*a*, 2007*b*).

PETROLOGY OF THE CAMBRIDGE DRILL CORE

A schematic log of the core is shown in Fig. 3 (following convention, the zero point of the cumulate stratigraphy is placed at the base of the exposed stratigraphy; i.e. at the HZ–LZa boundary). This log differs somewhat from that presented by Maaløe (1978, 1987), principally in the region –100 to +60 m stratigraphic height [i.e. including the unit b of Maaløe (1978)], in which Maaløe (1978, 1987) reported particular layers as occurring some tens of metres below our positions.

The HZ gabbros contain primocrysts of plagioclase and olivine, with interstitial augite oikocrysts, inverted pigeonite and oxides. The gabbros of LZa have the same mineralogy but augite becomes generally more granular through LZa towards the top of the core (see next section for details). Plagioclase has no preferred orientation in the lower parts of the drill core: the stratigraphic distribution of complex resorbed plagioclase cores (Fig. 2a), described by Maaløe (1976), has been outlined in an earlier section. We did not determine the relative proportions of ilmenite and magnetite as part of this study, but both Tegner *et al.* (2009) and Thy *et al.* (2009) determined, using least-squares approximations of bulk gabbro compositions, that ilmenite is generally more abundant than magnetite in the LZ.

Interstitial apatite is common throughout the core and the gabbros from the lowest parts of the intrusion

Table 3: Volumetric proportions (%) of the major phases in the Cambridge drill core

Sample	Height (m)	Zone	Plagioclase	Olivine	Total Fe–Ti oxides	Augite	Low-Ca pyroxene
3′ 11″	*197·8*	*LZb*	*55·9*	*4·3*	*1·7*	*26·3*	*10·5*
9′ 5″	*196·1*	*LZb*	*63·6*	*5·0*	*2·4*	*24·7*	*3·9*
10′ 11″	195·7	LZb	64·4	17·9	1·7	12·9	3·2
31′ 4″	189·4	LZb	66·8	10·8	0·6	16·1	5·8
39′ 3″	187·9	LZb	72·2	4·9	1·6	15·4	5·8
61′ 1″	180·4	LZb	75·7	9·2	0·8	11·9	2·5
71′ 1″	177·6	LZb	61·4	21·2	1·0	12·6	3·8
114′ 5″	164·0	LZa	62·5	14·2	0·6	17·2	5·5
115′ 4″	*163·9*	*LZa*	*35·8*	*45·0*	*1·8*	*11·1*	*5·5*
115′ 9″	163·8	LZa	45·4	36·3	1·6	10·7	6·0
122′ 2″	161·8	LZa	79·1	6·7	1·3	9·6	3·3
140′	156·3	LZa	59·7	17·4	0·8	19·6	2·5
152′ 3″	155·6	LZa	79·2	2·5	1·6	12·7	4·0
211′ 11″	134·4	LZa	74·9	11·0	0·4	10·1	3·6
262′ 7″	119·0	LZa	68·3	13·9	1·1	12·9	3·8
290′ 8″	110·0	LZa	73·1	6·5	1·4	15·8	3·1
300′ 1″	*107·5*	*LZa*	*60·3*	*17·0*	*2·2*	*15·1*	*3·9*
312′ 6″	103·8	LZa	69·5	12·8	0·8	14·1	2·8
322′ 6″	100·7	LZa	74·9	13·4	0·6	9·4	1·7
330′ 11″	98·1	LZa	67·9	16·6	0·9	10·6	4·0
338′ 5″	95·0	LZa	61·5	19·7	0·3	13·0	5·5
351′ 7″	91·8	LZa	67·6	12·5	0·7	14·6	4·6
361′ 5″	88·8	LZa	61·0	12·1	0·3	26·6	2·9
371′ 7″	85·7	LZa	71·8	18·9	0·3	6·2	2·8
389′ 7″	80·3	LZa	68·5	13·6	0·4	13·5	4·0
401′ 5″	*76·6*	*LZa*	*67·2*	*16·0*	*1·1*	*10·4*	*4·4*
411′ 5″	73·6	LZa	75·7	8·6	0·8	13·7	1·3
420′ 10″	70·7	LZa	75·3	11·7	0·7	9·2	3·1
438′ 4″	65·4	LZa	65·1	16·3	0·5	14·0	4·1
460′ 11″	58·5	LZa	76·2	14·4	0·8	4·6	4·0
490′ 11″	49·4	LZa	74·9	12·7	1·2	7·3	3·9
511′ 10″	43·3	LZa	65·0	20·5	0·7	9·9	3·9
522′ 1″	39·9	LZa	66·9	20·3	0·4	9·6	2·8
571′ 4″	24·8	LZa	88·3	5·5	1·2	2·0	3·0
581′ 1″	21·9	LZa	81·5	6·4	0·3	8·1	3·7
621′ 2″	9·7	LZa	74·1	7·5	0·2	15·6	2·7
651′ 2″	0·5	LZa	74·8	12·9	0·9	7·7	3·7
661′2″	–2·5	HZ	79·7	12·3	1·1	4·2	2·7
671′1″	–5·5	HZ	74·1	19·0	0·9	4·9	1·1
681′ 1″	–8·6	HZ	57·6	36·6	1·3	2·8	1·7
694′ 3″	–12·0	HZ	65·5	19·9	0·7	10·4	3·5
722′ 8″	–20·6	HZ	64·8	16·0	3·5	12·4	3·1
724′ 8′	*–21·9*	*HZ*	*64·1*	*20·5*	*2·3*	*2·5*	*9·7*
730′ 9″	–23·7	HZ	79·0	10·6	0·7	6·5	3·2
792′ 5″	–42·5	HZ	68·4	13·4	1·1	14·6	2·5
810′ 5″	*–48·0*	*HZ*	*68·9*	*7·3*	*1·1*	*19·9*	*2·7*
818′ 5″	–50·5	HZ	76·4	12·4	1·1	7·5	2·6
867′ 3″	–66·2	HZ	29·8	54·7	2·0	12·9	0·6
909′ 11″	–76·1	HZ	63·2	8·7	1·4	21·2	5·5
930′ 2″	–84·5	HZ	80·6	8·0	1·7	6·7	3·1
940′ 6″	–87·7	HZ	67·7	21·8	0·4	7·5	2·7
949′ 11″	–90·5	HZ	81·2	13·9	0·7	1·8	2·3
968′ 11″	*–96·3*	*HZ*	*57·0*	*28·8*	*0·2*	*11·5*	*2·4*
979′ 11″	–99·7	HZ	62·8	25·4	0·5	7·7	3·6
987′ 11″	–102·1	HZ	70·4	12·2	0·4	15·1	1·9
991′ 9′	–103·3	HZ	73·3	17·2	0·3	6·5	2·7
1019′ 11″	–111·9	HZ	72·9	12·9	1·9	9·1	3·2
1024′ 10″	*–113·4*	*HZ*	*67·2*	*12·6*	*2·3*	*5·9*	*10·1*
1029′ 11″	–114·9	HZ	71·6	5·0	0·3	21·2	1·9
1037′1″	–117·3	HZ	61·0	3·6	4·3	20·6	10·2
1049′ 11″	–121·0	HZ	78·8	8·1	0·6	5·3	7·2
1060′ 1″	–124·1	HZ	72·6	15·3	0·9	5·8	5·4
1122′3″	–143·1	HZ	71·0	5·7	2·1	17·6	3·6
1091′ 6″	–133·7	HZ	70·9	3·8	0·3	23·8	1·2

The sample number refers to depth in core, measured in feet and inches. Those data that appear in italics were previously reported by Nwe (1975).

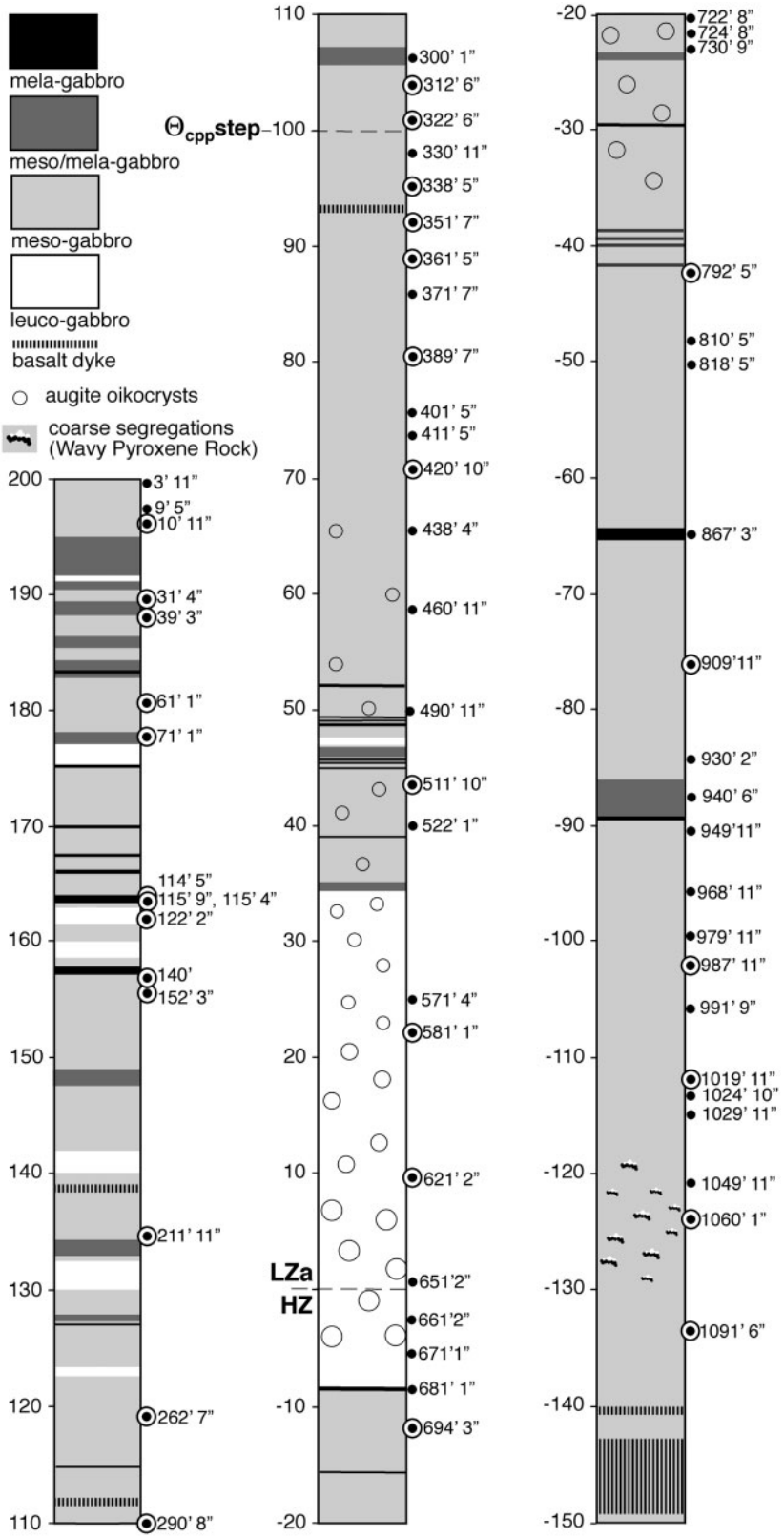

Fig. 3. Stratigraphy of the Cambridge Drill Core, with stratigraphic height given in metres. The distinctions between leuco-, meso- and mela-gabbro are not rigorously calibrated but serve to show where modal banding is present. The labelled dots give the position of the samples for which modal compositional data are presented in Table 2, and the labels give the depth in the core in feet and inches (as originally measured by the drill crew). Clinopyroxene morphology has been quantified for those samples with a circle around the dot. The boundary between HZ and LZa is shown, together with the stratigraphic position at which Θ_{cpp} increases in a stepwise way in response to the saturation of the bulk magma in augite.

Table 4: The volumetric proportions of the major phases in rocks from LZa and LZb described by Tegner et al. (2009)

Sample	Height	Zone	Plagioclase		Olivine		Total oxides		Augite		Low-Ca pyroxene	
458209	723	LZb	46·3	**48·4**	14·7	**15·5**	1·2	**0·6**	27·4	**33·2**	10·4	**2·3**
458208	703	LZb	57·5	**60·1**	0·9	**0·1**	0·6	**0·2**	37·5	**38·6**	3·5	**1·0**
458276	681	LZb	67·1	**67·8**	1·3	**2·3**	2·0	**2·4**	17·8	**21·5**	11·7	**6·0**
458206	634	LZb	52·7	**58·0**	5·0	**4·8**	1·4	**0·6**	30·7	**33·9**	10·3	**2·7**
458205	592	LZb	71·0	**70·7**	0·1	**0·4**	1·6	**1·4**	17·0	**24·9**	10·4	**2·6**
458203	558	LZb	59·5	**57·9**	3·2	**7·7**	1·2	**0·6**	28·1	**32·1**	8·0	**1·8**
458202	519	LZb	57·0	**58·0**	2·9	**3·4**	1·7	**2·4**	26·3	**31·2**	12·2	**5·0**
458201	488	LZb	48·1	**39·0**	16·6	**29·9**	1·4	**0·8**	21·4	**27·6**	12·4	**2·7**
458232	424	LZb	47·4	**42·0**	13·5	**21·6**	1·5	**1·9**	21·7	**30·6**	16·0	**3·9**
458231	367	LZb	63·2	**64·8**	1·7	**0·8**	1·2	**1·5**	22·4	**23·4**	11·4	**9·5**
458227	346	LZb	37·6	**44·6**	25·9	**25·2**	1·0	**1·2**	21·7	**23·1**	13·9	**5·9**
458226	294	LZb	61·5	**62·1**	4·9	**7·6**	0·7	**0·8**	24·9	**28·3**	8·0	**1·2**
458225	221	LZb	58·8	**60·0**	1·7	**8·0**	2·2	**1**	22·1	**26·2**	15·2	**4·8**
458224	177	LZb	54·6	**54·6**	3·2	**6·3**	1·9	**1·7**	26·2	**31·5**	14·2	**5·9**
458221	175	LZb	57·9	**60·2**	5·8	**8·0**	2·1	**2·3**	14·5	**23·3**	19·7	**6·2**
458220	173	LZa	81·0	**84·0**	0·1	**3·1**	1·2	**1·2**	6·5	**7·4**	11·2	**4·3**
458219	161	LZa	64·7	**68·2**	4·4	**7·1**	1·8	**0·2**	14·6	**18·1**	14·5	**6·4**
458217	137	LZa	61·7	**65·0**	7·1	**10·2**	2·2	**0·7**	11·6	**16·6**	17·5	**7·5**
458215	115	LZa	62·6	**62·3**	4·5	**14·9**	2·3	**0·9**	9·8	**16·1**	20·8	**5·8**
458214	107	LZa	50·0	**51·6**	14·5	**18·1**	3·1	**2·7**	9·4	**19·3**	23·1	**8·3**
458213	84	LZa	70·2	**65·7**	7·1	**6·1**	1·7	**1·1**	11·6	**20·1**	9·4	**7·0**
458212	54	LZa	60·9	**65·9**	8·2	**12·1**	2·2	**2·3**	15·0	**13·2**	13·7	**6·5**

The first set of numbers were calculated from weight proportions given by Tegner *et al.* (2009) assuming a density of 2·7 g cm^{-3} for plagioclase, 3·7 g cm^{-3} for olivine, 3·3 g cm^{-3} for augite and low-Ca-pyroxene, 4·7 g cm^{-3} for ilmenite and 5·2 g cm^{-3} for magnetite. The second set of numbers for each sample (those in bold type) were derived directly from image analysis of thin sections.

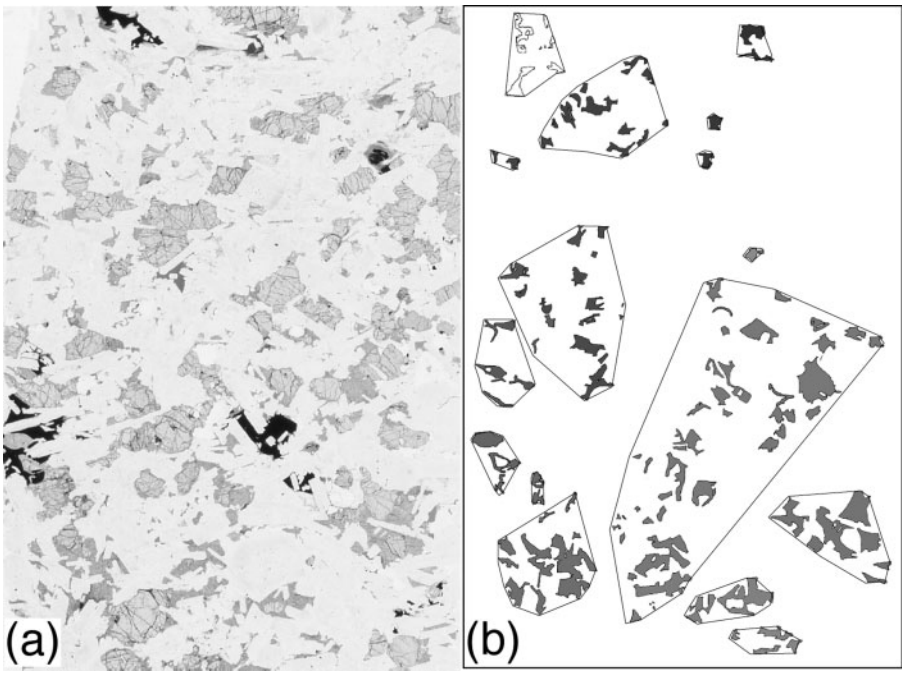

Fig. 4. Sample 118737, from –124 m stratigraphic height (1060′1″ depth in the drill core). (a) Scanned image, and (b) line drawing from the scanned image, showing the distribution of augite within the thin section. Each image is 18 mm wide. Each shaded patch is termed a domain: a single domain corresponds to a single augite crystal only when augite forms highly compact grains. When oikocrysts are cut by the section, they appear as clusters of many domains, each identifiable as part of the oikocryst by their identical lattice orientation, discernible by extinction position and birefringence. The polygons show the outer bound (estimated by eye) of each oikocryst in the plane of the section.

contain more apatite than any other rock in the Layered Series, except for those above UZb (McBirney, 1989*b*). Biotite forms large interstitial grains and rims around interstitial oxide grains (Fig. 2b). Some (inverted) pigeonite is present (Fig. 2c) and is likely to have formed by reaction between olivine and evolved interstitial liquid. A brown amphibole locally forms rims around clinopyroxene grains (Fig. 2d). Pockets of late-stage silicic liquid crystallized as granophyric intergrowths of quartz and K-feldspar.

The basal 7 m of the core contains a minor, late-stage, fine-grained dolerite intrusion. Another late dolerite dyke (50 cm thick) occurs at about –140 m. The lowermost gabbros are homogeneous with no modal layering. Coarse-grained, subhorizontal segregations of plagioclase with augite oikocrysts are scattered, with ~1 m spacing, between –120 and –130 m, perhaps corresponding to the Wavy Pyroxene rock of the MBS. Modal layering is only locally present and is very poorly defined in the lowermost 140 m of the core.

The core is macroscopically featureless meso-gabbro between –120 and –89·2 m. Overlying this region (i.e. at –89 m) is a 30 cm thick layer of mela-gabbro with an upper surface marked by an abrupt upwards transition to meso-gabbro. This is followed by a gradual grading to more mafic gabbro, which has a sharp upper contact at –85 m against a relatively coarse-grained and leucocratic gabbro. There is a single well-defined, 75 cm thick olivine-rich layer with its base at –65 m. This layer comprises subequant to rounded olivines enclosed by pyroxene (predominantly augite) oikocrysts (Fig. 2e), with subordinate plagioclase—it is not finer-grained relative to the under- and overlying horizons [it is probable that this olivine-rich layer is the unit a of Maaløe (1978)]. The region between –44 and –9 m is marked by sparse and poorly defined variations in modal composition, with some scattered augite oikocrysts.

A 15 cm thick mafic layer, in which olivine is the predominant mafic phase, occurs at –8·8 m and, in contrast to the layer at –65 m, its base is marked by an abrupt decrease in average olivine grain-size from 0·9 to 0·3 mm (Figs 2f and 5a). The grain size remains low for about 20 m of stratigraphy and then climbs back to the original value through the overlying 30 m; over the same distance the mode grades towards more plagioclase-rich compositions with large scattered augite oikocrysts (Fig. 5c and Table 3). Some 3 m above the abrupt decrease in grain size, Θ_{cpp} increases significantly to a localized peak before returning to lower values by ~12 m stratigraphic height (Fig. 5b). The top of this leucocratic layer is at 34·5 m stratigraphic height. The region between 45 and 52 m is the first zone of relatively well-defined modal layering on a decimetre scale, with layers comprising thin (5 cm) relatively mafic bases grading into a plagioclase-rich upper part. This layered horizon is associated with an abrupt decrease of the anorthite content of plagioclase (Maaløe, 1976; although he placed it at ~30 m) and disruption of the layering in exposed outcrops, attributed to the onset of chamber-wide convection (Maaløe, 1987). This region also corresponds to the base of one of the three subdivisions of the core suggested by Nwe (1975). She found that the poikilitic habit of augite common in the lower part of the core (her zone I, Fig. 6) begins to grade towards a sub-poikilitic habit above 16 m stratigraphic height. She described the region of the core between 46 and 107 m as a transitional zone (her zone II) between troctolitic and the overlying gabbroic cumulates, characterized by granular augite, of her zone III (Fig. 6). Just above 100 m is a change from a granular, pepper-and-salt, appearance to a slightly more melanocratic rock, although the gabbro returns to meso-gabbro within 10 m or so. This is the point at which the median dihedral angle increases in a stepwise fashion (Holness *et al.*, 2007*a*) (Fig. 6). The uppermost 100 m of the core contains poorly defined layers on the 1–3 m length-scale, defined by variation in the augite mode (Maaløe, 1987) (Fig. 3).

MICROSTRUCTURES IN THE DRILL CORE

Augite morphology

The variation of augite morphology with stratigraphic height through the drill core is shown in Fig. 7. The number of optically distinct augite grains in each thin section, *n*, divided by the area occupied by augite, *A*, provides a comparative measure of how many separate nuclei exist per unit volume of augite. A low value of *n*/*A* denotes that the clinopyroxene in the sample forms few large grains (i.e. in the particular case of the drill core gabbros, clinopyroxene predominantly forms oikocrysts), whereas a high value of *n*/*A* denotes that the clinopyroxene in the sample forms many small grains. The value of *n*/*A* in the core is generally low until about 80 m (Fig. 7a). Above this level *n*/*A* is variable, and several samples have very high values. However, apart from these peaks, the underlying trend is generally one of continually increasing *n*/*A*. A similar pattern is seen in the variation of the average size of the domains (Fig. 7b). This is a simple measure of the size of each identifiable patch of augite, irrespective of whether these patches are in optical continuity with others; for a cumulus phase this offers a measure of the size of single cumulus grains whereas for an interstitial phase it is commensurate with the size of the pores in which it grew (and thus provides information on the relative timing of compaction/overgrowth of the plagioclase-dominated mushy layer and the nucleation and growth of the interstitial phase).

A measure of the compactness of single clusters of domains in optical continuity is shown in Fig. 7c. Compactness is the total area of the enclosed domains divided by the area of the polygon enclosing each oikocryst (or cluster of optically continuous domains; see Fig. 4); it is essentially a measure of the area comprising pyroxene within the outline of each oikocryst. A single, perfectly convex grain thus has a compactness of 1·0 whereas an oikocryst (or a cumulus grain with some orthocumulus overgrowth) has lower compactness. Compactness is variable but generally low in the lower 150 m of the core, and increases almost continuously upwards from 0 m stratigraphic height.

Dihedral angles in the drill core

The variation of Θ_{cpp} through the core was first described by Holness *et al.* (2007*a*), and these earlier data, based on populations of only 30 measurements

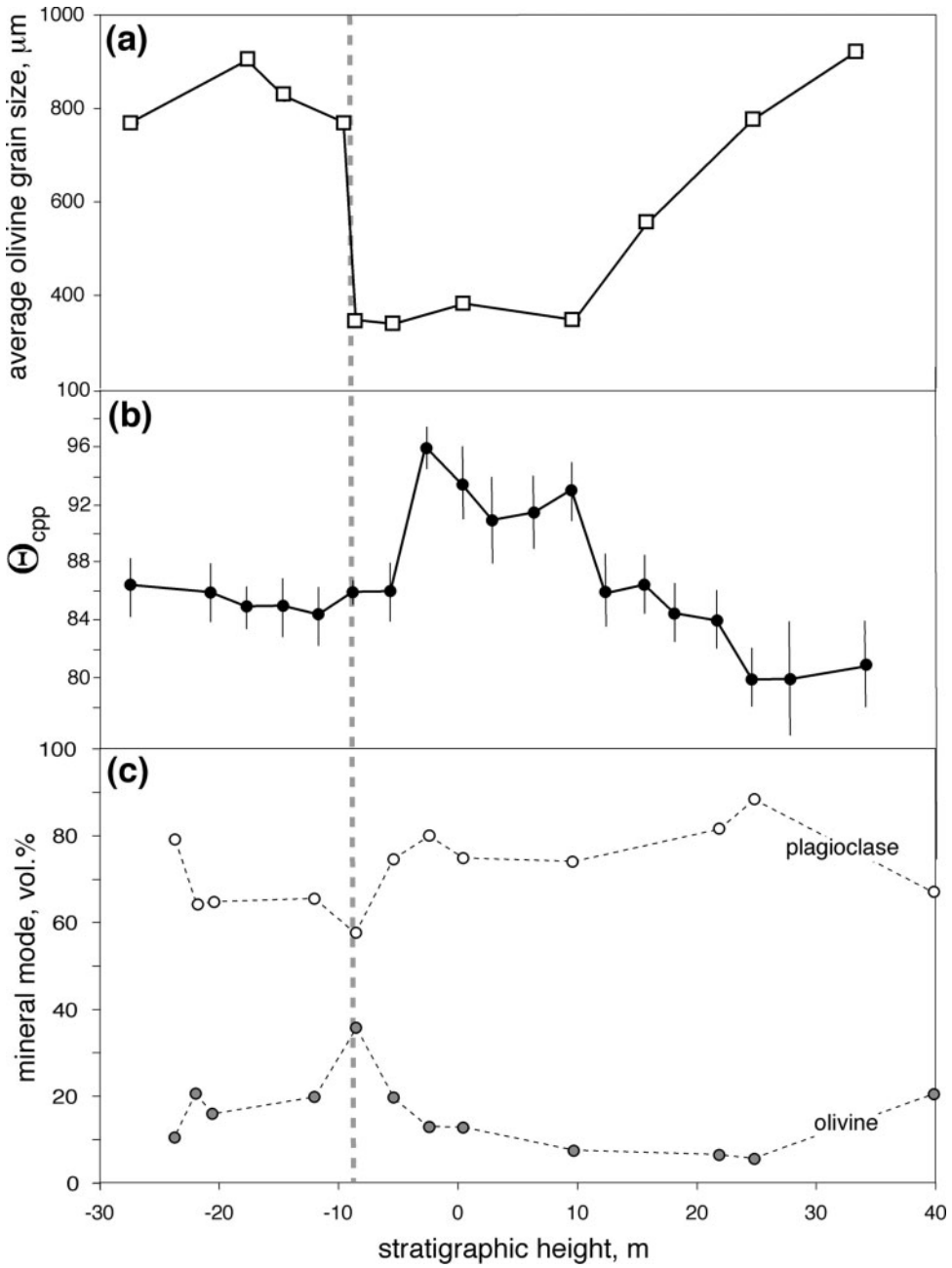

Fig. 5. (a) The average olivine grain size in the Cambridge Drill Core in the region of 0 m stratigraphic height (the HZ–LZa boundary). The abrupt reduction in grain size at –8·6 m occurs within an olivine-rich band. The dashed grey line at –8·8 m shows the position of the base of this band. (b) Variation of Θ_{cpp} in the same region of the core. Each dot represents the median of a population of between 30 and 60 measurements, with the 95% confidence intervals about the median calculated according to Stickels & Hucke (1964). (c) The stratigraphic variation of the mode of plagioclase and olivine. Data are given in Table 3.

per sample with large associated uncertainties, are given in Table 1 and shown in Fig. 6, together with the data collected as part of the present study.

Θ_{cpp} in the drill core is characterized by low values in the lowermost few tens of metres, with a marked peak at –120 m. Values then drop to about 85° until –2·5 m where they increase to form a broad peak (across 12 m of stratigraphy) over ~90° before decreasing again to ~80° (Fig. 5). There is a well-defined stepwise increase at 100 m to ~100°. The short-wavelength variation of Θ_{cpp} through the core is generally not as great as previously reported by Holness *et al.* (2007*a*).

BULK ELEMENT CONCENTRATIONS IN THE DRILL CORE

Major elements

The variation of major elements is dominated by the modal proportions of plagioclase, olivine, Ca-rich pyroxene, low-Ca pyroxene and Fe–Ti oxides. This is

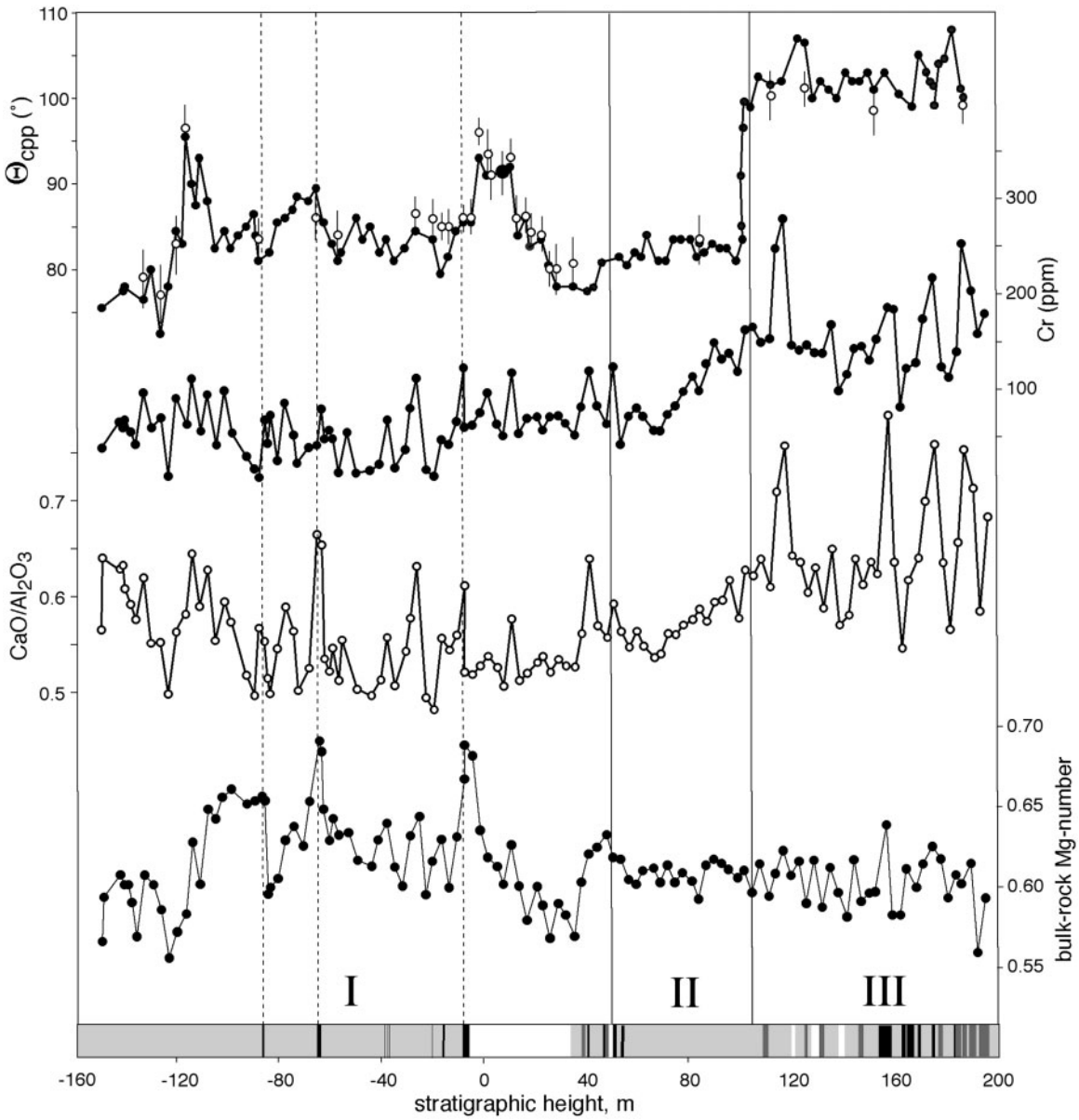

Fig. 6. Variation of Θ_{cpp}, and bulk-rock Cr content, CaO/Al_2O_3 and Mg-number as a function of stratigraphic height in the Cambridge Drill Core. The black dots give the values of Θ_{cpp} published by Holness *et al.* (2007*a*), based on populations of 30 measurements, whereas the open circles indicate our values determined from a subset of the samples with a sufficiently large population to reduce the 95% confidence interval about the median to below ±3·5° [calculated according to Stickels & Hücke (1964) and shown as vertical lines through each data point]. A schematic stratigraphic log is provided along the *x*-axis (shaded as in Fig. 3). The vertical dashed lines at –85, –64 and –8·8 m correspond to horizons linked to magma influx. The three subdivisions of Nwe (1975) (labelled I, II and III) are shown by continuous vertical lines.

shown by the anti-correlation between the group of elements Si, Al, Ca, Na and K associated with feldspar and the elements found in mafic phases (Fe, Mn, Mg) (Table 5). The stratigraphic variation of the three major elements CaO, Al_2O_3 and MgO included in plagioclase and olivine is shown in Fig. 8 (with the variation of bulk-rock Mg-number, calculated using FeO_{tot}, shown in Fig. 6). The variation of Na_2O (not shown, data in Table 1) is strongly correlated with that of Al_2O_3 (Table 5), whereas that of FeO_{tot} (not shown, data in Table 1) correlates with that of MgO (Table 5). The positions of the mafic layers at –65 and –8·8 m, with another at 157 m, are marked by high MgO, and low Al_2O_3 and CaO, whereas the plagioclase-rich zone above –8·8 m is marked by low MgO, and high Al_2O_3 and CaO. The modal layering in the uppermost parts of the core results in significant variability of the major elements. The absence of any correlation between Fe–Ti oxide and plagioclase modes (Table 3), together with the very minor oxide content of these rocks, means that the bulk-rock FeO_{tot} and MgO concentrations are controlled almost entirely by olivine and pyroxene.

The bulk-rock Mg-number varies from 0·56 to 0·69, with the greatest variability below 40 m stratigraphic

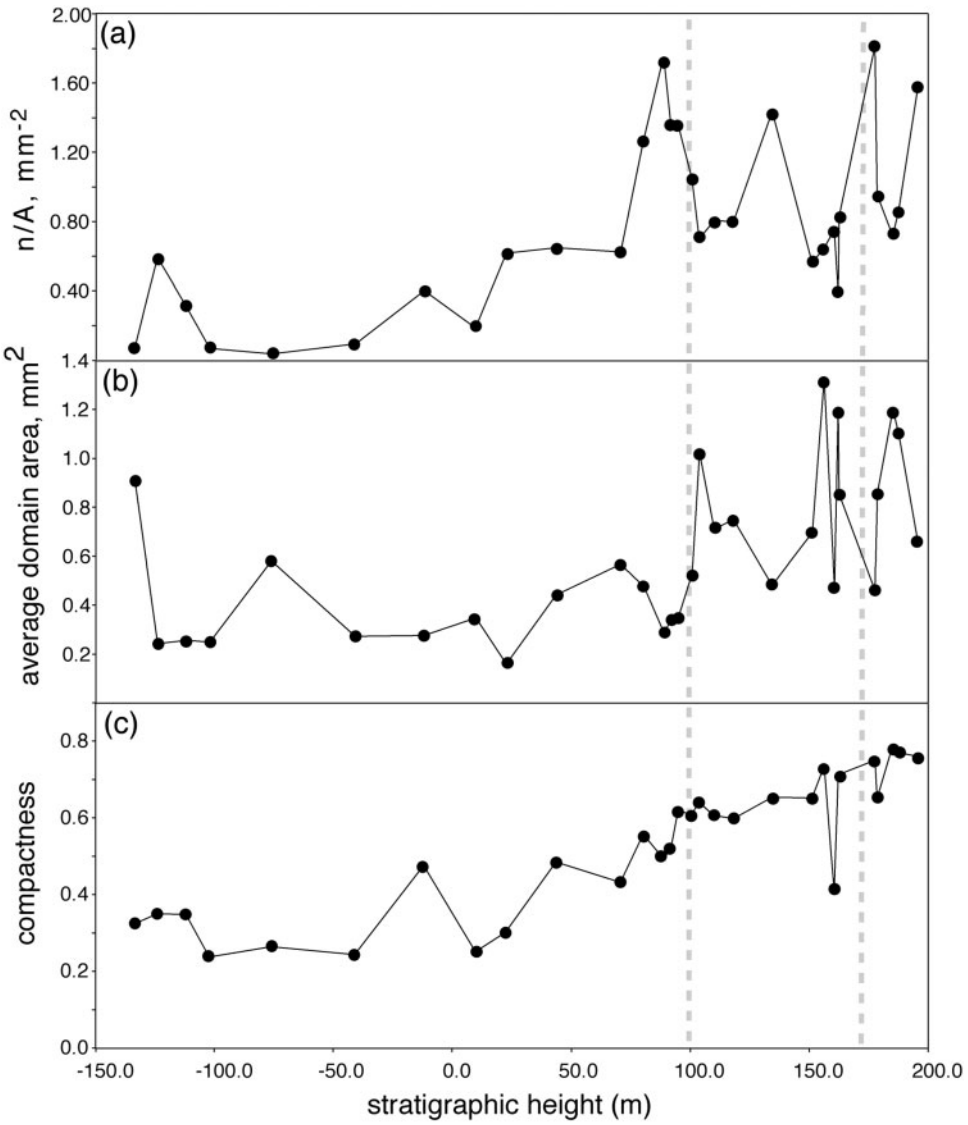

Fig. 7. The variation of augite morphological parameters with stratigraphic height in the drill core: (a) the number of optically discernible grains (either oikocrysts or cumulus; *n*) per unit of area of the thin section occupied by augite (*A*); (b) the average size of single domains of augite cut by the thin section—this provides an indication of the size of the pores into which intercumulus augite grew or of the size of cumulus grains; (c) the compactness of each optically distinct augite grain or oikocryst. The Tegner *et al.* (2009) position of the LZa–b boundary at 175 m (see text for details) and the position of the stepwise change in Θ_{cpp} at 100 m are shown by dashed grey lines.

height. There is no correlation between Mg-number and any of the other compositional variables (Figs 6, 8, 9 and 10), so these variations must primarily reflect changes in mafic mineral composition. The two well-defined mafic layers at –65 and –8·8 m are marked by high bulk-rock Mg-number, whereas that at about –89 m is marked by a drop in Mg-number. The olivine-rich layer at –8·8 m is associated with high Θ_{cpp}, and the increase in Mg-number at about –120 m is also associated with a peak in Θ_{cpp} (Fig. 6).

Minor elements

Because neither Fe–Ti oxides, apatite, amphibole, biotite nor K-feldspar are liquidus phases in the HZ and LZ, the variation in bulk-rock Ti, P and K contents provides information about the amount of liquid remaining in the mush at the point of saturation of the interstitial liquid in these minerals. Caveats for this approach are (1) that because plagioclase contains appreciable amounts of K_2O [0·25–0·30 wt %, Namur *et al.* (2014)] the correlation of K_2O bulk-rock concentration with interstitial liquid is not strong, and (2) that augite can contain appreciable Ti, so once augite becomes cumulus bulk-rock Ti is likely to be controlled mainly by the augite mode.

In general, there is greater variability of P_2O_5 and TiO_2 compared with that of K_2O, especially in the stratigraphic interval 40–120 m (Fig. 9). Compositions are generally more variable in the upper ~80 m of the core, corresponding to the region with marked modal

Table 5: Correlations between major and trace elements, calculated for all drill core samples

	SiO_2	TiO_2	Al_2O_3	Fe_2O_3	FeO	MnO	MgO	CaO	Na_2O	K_2O	P_2O_5	Ba	V	Cr	Ni	Cu	Zn	Sr	Y	Zr
SiO_2	1																			
TiO_2	0·17	1																		
Al_2O_3	0·69	–0·11	1																	
Fe_2O_3	0·06	0·32	–0·22	1																
FeO	–0·86	–0·03	–0·89	–0·08	1															
MnO	–0·80	0·04	–0·94	0·07	0·96	1														
MgO	–0·91	–0·21	–0·86	–0·02	0·93	0·90	1													
CaO	0·91	0·12	0·69	0·09	–0·90	–0·81	–0·89	1												
Na_2O	0·86	0·19	0·84	–0·02	–0·85	–0·89	–0·93	0·73	1											
K_2O	0·53	0·41	0·39	0·07	–0·44	–0·37	–0·59	0·35	0·65	1										
P_2O_5	0·19	0·17	0·07	–0·01	–0·04	–0·06	–0·19	–0·04	0·32	0·63	1									
Ba	0·37	0·59	0·00	0·30	–0·15	–0·08	–0·35	0·20	0·39	0·74	0·52	1								
V	0·27	0·75	–0·34	0·49	–0·01	0·15	–0·13	0·30	0·02	0·28	0·09	0·57	1							
Cr	0·27	0·30	–0·42	0·35	0·06	0·14	0·02	0·25	–0·05	–0·06	–0·02	0·24	0·70	1						
Ni	–0·92	–0·27	–0·72	–0·06	0·86	0·81	0·95	–0·90	–0·87	–0·55	–0·15	–0·44	–0·30	–0·16	1					
Cu	–0·06	0·47	–0·23	0·10	0·27	0·27	0·02	–0·24	0·07	0·50	0·60	0·61	0·32	0·04	–0·05	1				
Zn	–0·70	0·08	–0·83	0·11	0·89	0·87	0·78	–0·76	–0·72	–0·34	0·00	–0·02	0·12	0·17	0·71	0·38	1			
Sr	0·71	–0·03	0·96	–0·19	–0·88	–0·93	–0·88	0·69	0·88	0·46	0·11	0·14	–0·26	–0·38	–0·79	–0·11	–0·82	1		
Y	0·58	0·43	0·07	0·25	–0·28	–0·23	–0·44	0·38	0·48	0·69	0·60	0·79	0·57	0·42	–0·55	0·50	–0·17	0·20	1	
Zr	0·23	0·63	0·00	0·19	–0·06	–0·02	–0·25	0·04	0·32	0·77	0·60	0·80	0·46	0·07	–0·31	0·70	0·00	0·13	0·76	1

layering. There is a positive excursion in both K_2O and P_2O_5 just below the –8·8 m mafic layer (in sample 722′8″ at –20·6 m stratigraphic height, Table 1), although this is not accompanied by an excursion in TiO_2. The base of the –8·8 m mafic layer is marked by an abrupt decrease in the concentration of P_2O_5, TiO_2 and K_2O (Fig. 9), with a gradual increase through the overlying plagioclase-rich zone.

Trace elements

Correlations between the trace and major elements (Table 5) can be used to determine which minerals host the trace elements. Ni and Zn correlate strongly with Fe, Mn and Mg, consistent with these elements being partitioned into olivine. V is strongly correlated with Ti and weakly with Fe^{3+}, suggesting titanomagnetite as the main host. Cr is strongly correlated with V, consistent with a titanomagnetite host, although it is also partitioned into augite. Sr is strongly correlated with Si, Al, Ca and Na, consistent with a plagioclase host. Cu, and Ba correlate with K and Ti, and the likely host minerals are amphibole and biotite (e.g. Class & Goldstein, 1997). Y and Zr both correlate with K_2O and P_2O_5 whereas Y is more strongly correlated with TiO_2 than Zr. The correlation of Y, Zr, Cu and Ba with P_2O_5 is consistent with their recording the proportion of late-stage evolved liquids.

The stratigraphic variation of bulk-rock Cr (in ppm) is shown in Fig. 6. It displays a poorly defined stepwise increase at –8·8 m, with high and constant values relative to those in the underlying parts of the core. Bulk-rock Cr shows a gradual and well-defined increase in zone II of Nwe (1975) towards generally high but variable values in her zone III.

The stratigraphic variation of Y and V is shown in Fig. 10 (data in Table 2). A marked decrease in Y and V occurs in the vicinity of the –8·8 m olivine layer, but it occurs in the sample analysed at –8·6 m, and not in the olivine-rich sample from –8·7 m. For Y this is followed by a gradual increase in concentration through the overlying plagioclase-rich region to higher values in zones II and III (Fig. 10). The bulk-rock concentration of V increases continuously through zone II from the minimum at –8·6 m, with variable values in zone III (Fig. 10).

MINERAL COMPOSITIONS

The stratigraphic variation of olivine composition was examined in detail from the base of the core up to 25 m stratigraphic height to investigate the history of magma chamber filling. Selected samples from the reference profile described by Tegner *et al.* (2009) were also analysed (P. Thy & C. Tegner, unpublished data), and the average Fo contents of these samples are shown in Fig. 11, together with data from Nwe (1975). Forsterite contents of randomly chosen grains generally vary by $<$0·02 within each sample, although there are several notable exceptions to this, at –119·5, –117·3 and –108·8 m, where different olivine grains in the same sample vary in composition by as much as 10 mol % Fo (Fig. 11). Forsterite contents are highly variable in the lower part of the core but generally correlate with the Mg-number of the bulk-rock (Fig. 12).

The olivine analyses of Nwe (1975) fall within the range we observed in the lower part of the core (Fig. 11). Preliminary data for the suite described by Tegner *et al.* (2009) (P. Thy & C. Tegner, unpublished data) show broadly decreasing forsterite contents with increasing stratigraphic height.

The compositions of randomly chosen plagioclase cores were measured in samples from the HZ, together with selected samples from the Tegner *et al.* (2009) reference profile (P. Thy & C. Tegner, unpublished data). There is no discernible trend in the data from the drill core (Fig. 11), although there is a general decrease in An content in the Tegner *et al.* (2009) samples from the lower part of the exposed Layered Series. The data fall in the same range as those of Maaløe (1976) (Fig. 11).

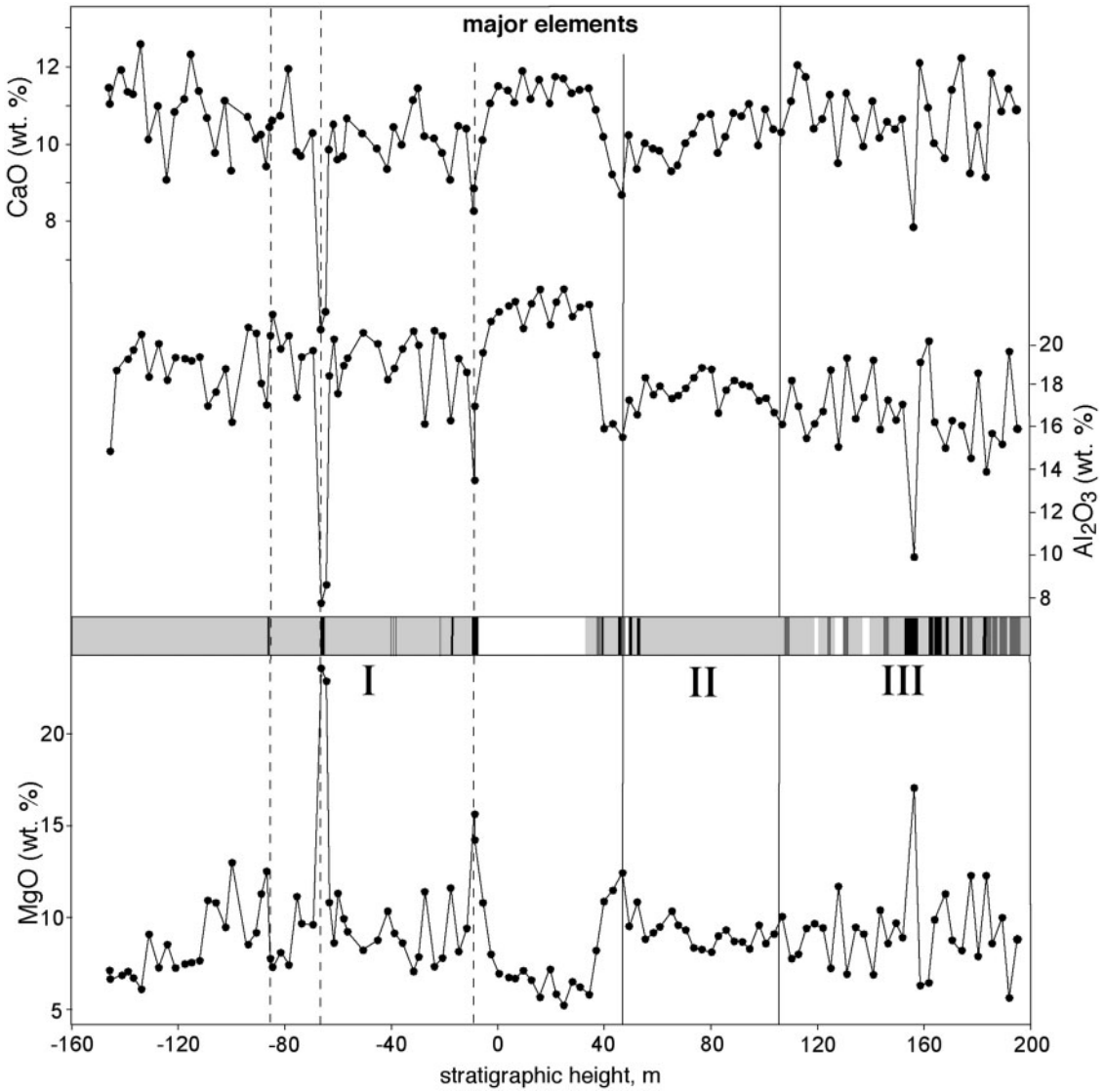

Fig. 8. The bulk-rock variation of CaO, Al_2O_3 and MgO (wt %) with stratigraphic height in the Cambridge Drill Core. A schematic stratigraphic log is indicated. The vertical lines are subdivisions according to the caption to Fig. 6.

Given the interstitial nature of the Ca-rich pyroxene through much of the Skaergaard drill core we chose not to undertake an exhaustive study of pyroxene compositions that would develop the work of Nwe (1975, 1976). Instead, we measured major element concentrations in pyroxenes from six samples and amalgamated these with a further 10 analyses presented by Nwe (1975). We also investigated the Cr content of augite in 12 samples from the drill core, together with three samples from the Tegner *et al.* (2009) suite, to determine if trace element concentrations can be used to detect the stratigraphic position at which augite becomes cumulus (Cr is compatible in Ca-rich pyroxene and Fe–Ti oxides).

With the exception of the sample at –133·7 m (1091′6″), the Mg-number of Ca-rich pyroxene correlates strongly with the forsterite content of the coexisting olivine (Fig. 13a), with no apparent difference observed in the strength of the correlation between samples collected above 100 m stratigraphic height [the point at which Nwe (1975, 1976) suggested augite is transitional to cumulus] and those below. It should be noted that the correlation between olivine and augite compositions appears to be independent of the correlation between olivine composition and the bulk-rock Mg-number; whereas sample –133·7 m lies off both trends, the sample at –143·1 m lies on the former but not the latter.

The Cr content of single augite grains is highly variable, with significantly lower values at the grain edges. It is difficult to be certain of the 3-D geometry of non-euhedral grains, particularly oikocrysts, and to know how far each analysis point is from the grain edge. In Fig. 13b we show all Cr analyses, but highlight the data point in each sample with the lowest concentration of the highly incompatible element Lu. This data point is most likely to be representative of the core of each grain. The maximum Cr content in each sample is very low in the lower part of the drill core, with a major

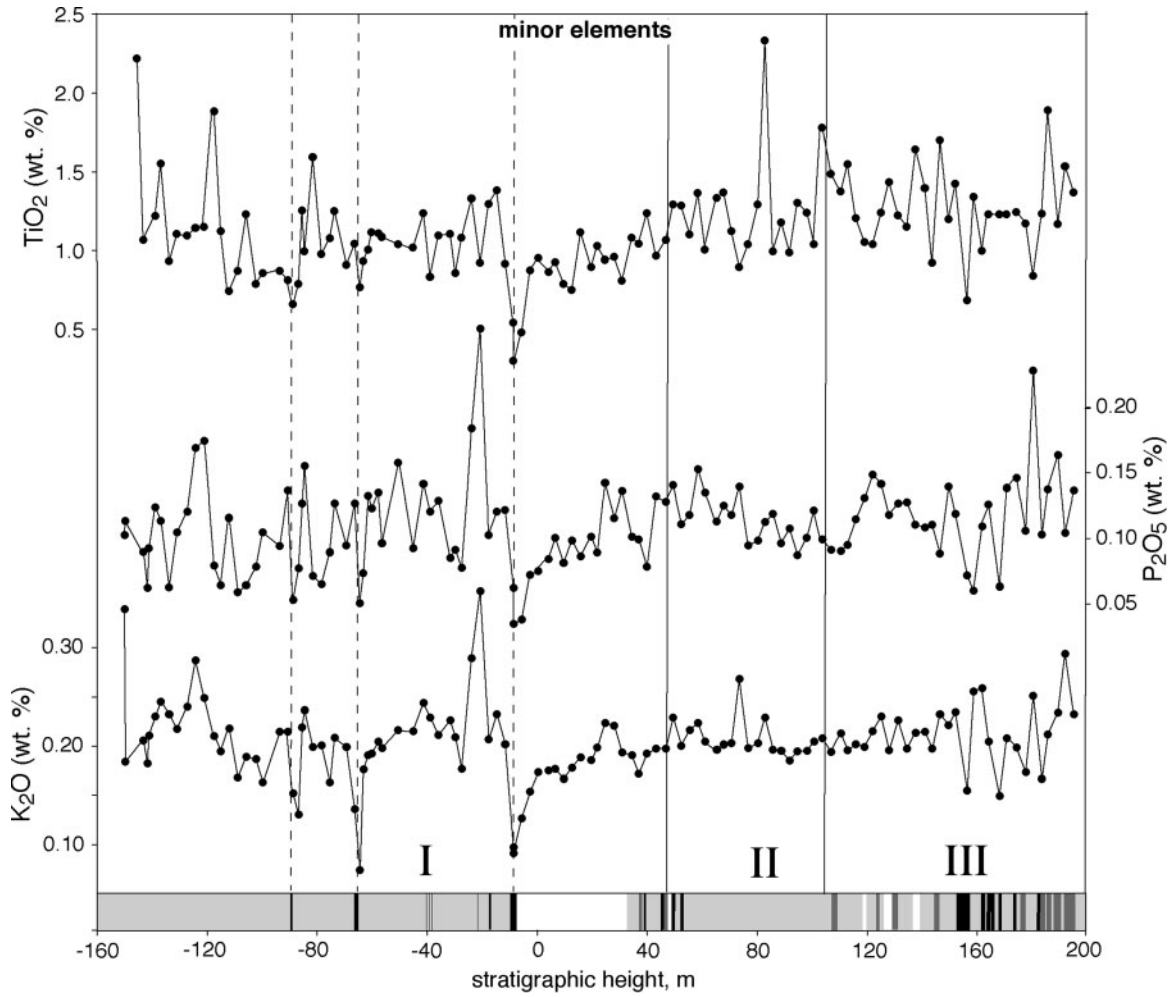

Fig. 9. The bulk-rock variation of TiO_2, P_2O_5 and K_2O (wt %) with stratigraphic height in the Cambridge Drill Core. A schematic stratigraphic log is indicated. The vertical lines are subdivisions according to the caption to Fig. 6.

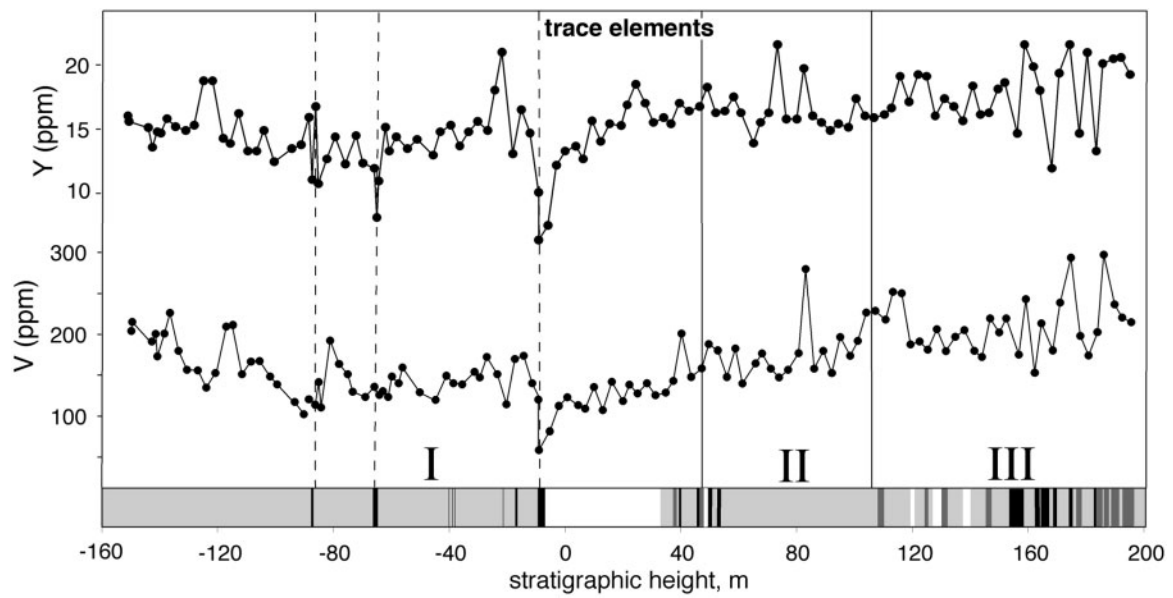

Fig. 10. The bulk-rock variation of Y and V with stratigraphic height in the Cambridge Drill Core. A schematic stratigraphic log is indicated. The vertical lines are subdivisions according to the caption to Fig. 6.

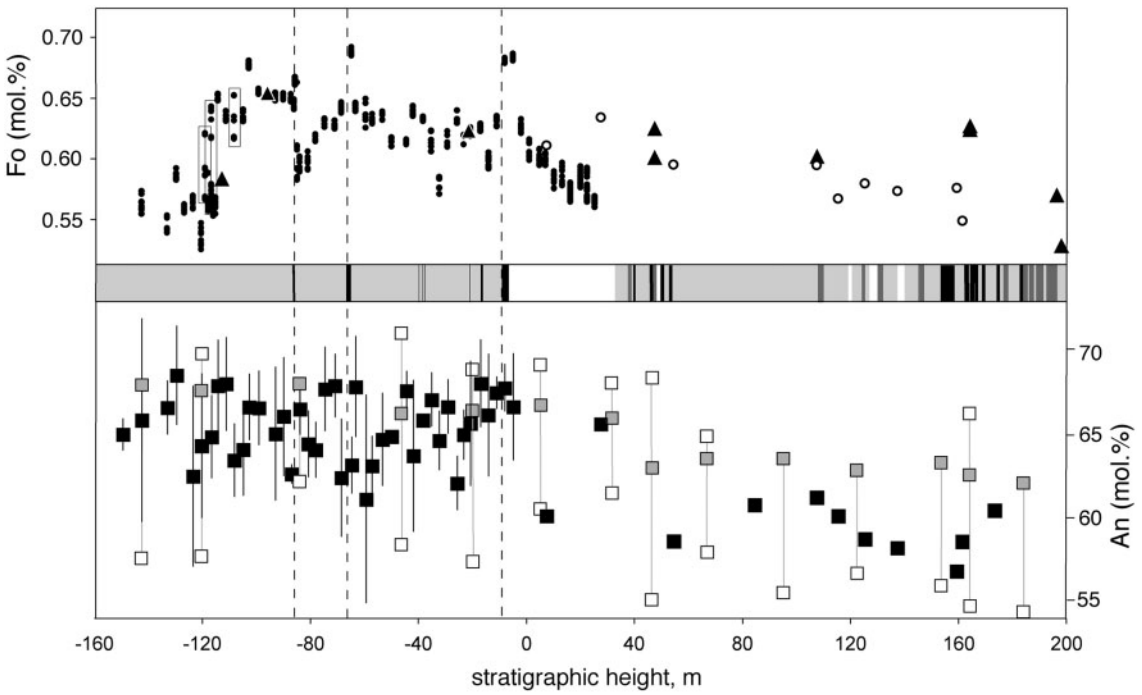

Fig. 11. Variation of olivine forsterite content (Fo) and plagioclase anorthite content (An) with stratigraphic height. The small black dots give the forsterite contents for single analyses of olivine grain cores in the Cambridge Drill Core (this study). The black triangles are the data of Nwe (1975) and the open circles are average olivine compositions for selected samples through the reference profile described by Tegner *et al.* (2009). The samples with boxes showing the range of forsterite compositions are those with an unusually wide range of core compositions and are likely to record olivine-phyric magma influxes. Black squares are the average plagioclase core compositions obtained in this study, and the lines through each black square show the standard deviation of the dataset for each sample. The grey and open squares are the data of Maaløe (1976) from the drill core, with the grey squares showing the average core compositions and the open squares showing the extent of the range of compositions of both normal and reverse rims. If only normal rims are shown, then the reverse rims are absent from that sample [see Maaløe (1976) for further details].

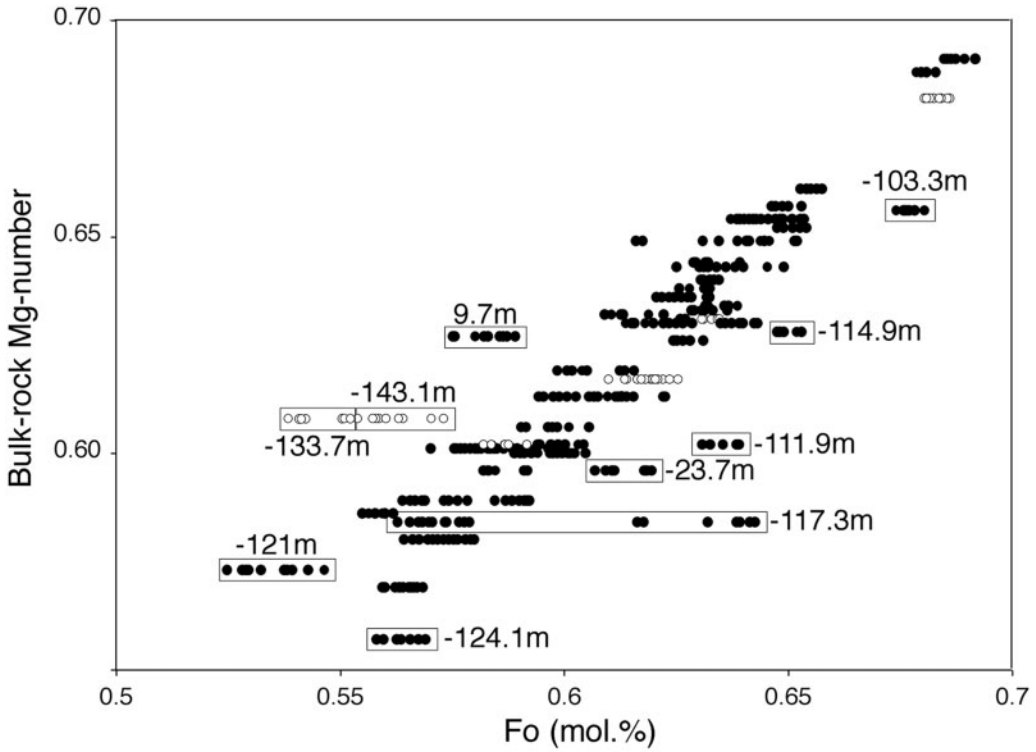

Fig. 12. Olivine forsterite content as a function of bulk-rock Mg-number. The data form a strong correlation with the exception of six samples with higher than expected Fo content and four with lower than expected Fo. That at –117·3 m contains a polymodal olivine population. Data marked as open circles are averaged and plotted vs the average Mg-number of coexisting augite in Fig. 13a.

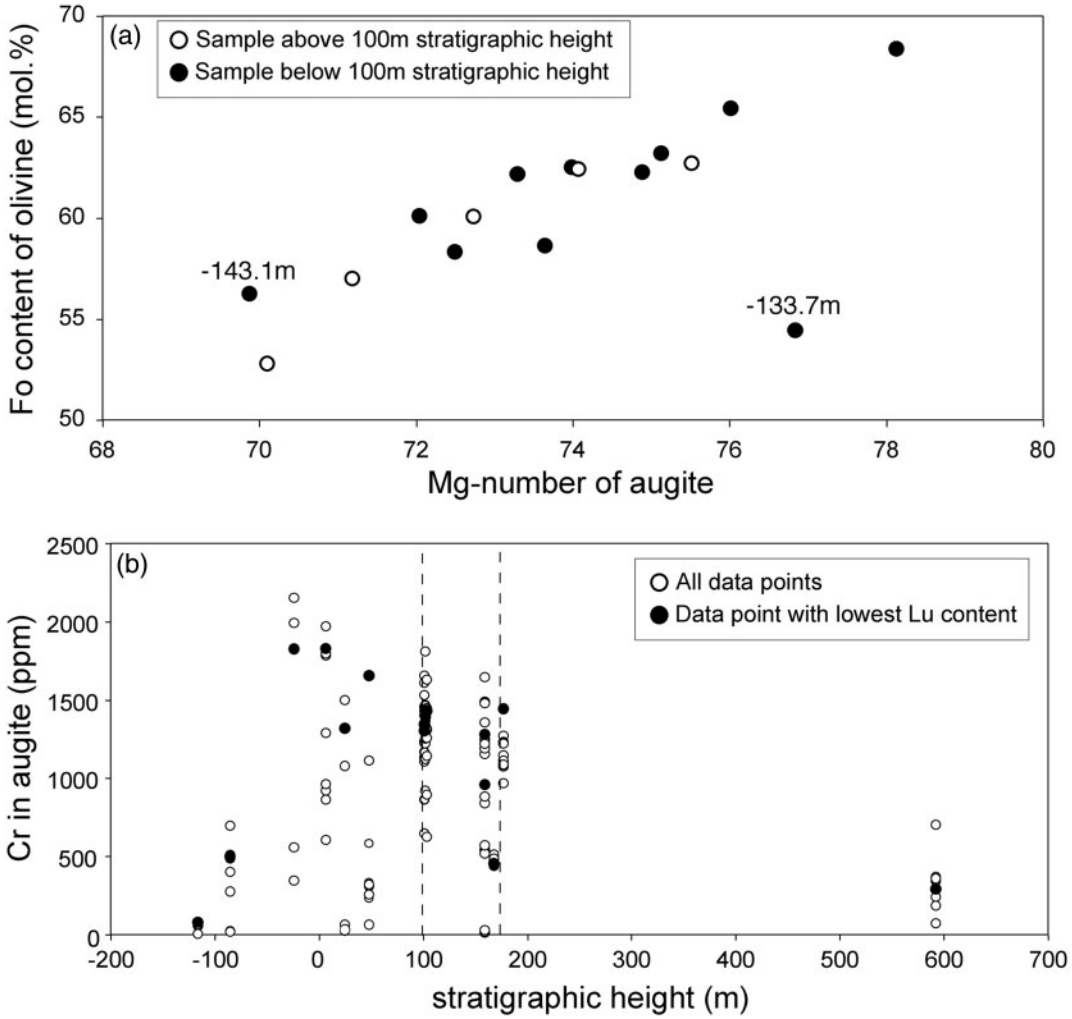

Fig. 13. (a) Forsterite content of olivine as a function of the Mg-number of coexisting augite. Data from Nwe (1975) are shown in addition to data from this study. The strong correlation between the two minerals and that no distinction can be made between mineral pairs from below and above 100 m stratigraphic height [the base of division II of Nwe (1975, 1976)] should be noted. The labelled samples are those that fall off the main trend in Fig. 12. (b) Cr concentration in augite through the drill core and lower part of the Layered Series. The open circles show all data, whereas the filled black circles indicate the data point within any sample with the lowest Lu concentration.

increase between –85 and –24 m. Above this point it decreases steadily to the highest sample we measured at 592 m (which is towards the top of LZb). The data point with lowest incompatible element content shows similar patterns, although with more variability.

DISCUSSION

Critical to the discussion of our results is whether or not the compositional record in the cumulates is essentially unmodified after crystal accumulation. Can we interpret variations in olivine composition and bulk-rock Mg-number to deduce the history of the magma chamber? Given the wide range in observed bulk-rock P_2O_5 concentrations (i.e. a probably wide range of trapped liquid volumes), the strong correlation between augite and olivine compositions shown in Fig. 13a suggests that there has been only rather minor modification of Mg:Fe ratios in cumulus olivine by a trapped liquid shift (Barnes, 1986). Exceptions to this are the four samples with apparently anomalously low-Fo olivines shown in Fig. 12 (9·7, –143·1, –133·7 and –121 m), which are possible candidates for significant reduction of the Mg:Fe ratio in olivine owing to trapped liquid shift. These four samples have relatively low olivine modes coupled with either high P_2O_5 (–121 and –133·7 m) or high modes of interstitial pyroxenes (9·7 and –143·1 m) (Table 3) consistent with a significant re-equilibration of cumulus olivine with a rather evolved interstitial liquid. We conclude that the stratigraphic variation of both olivine composition and bulk-rock Mg-number are sufficiently unmodified that we can use them to interpret variations in the composition of the bulk magma from which the cumulates crystallized.

That plagioclase compositions do not appear to show the same features as the coexisting olivine is interesting. We suggest that the absence of a clear signature of mineral compositional variation from the

plagioclase is because our data are simply not detailed enough. Maaløe (1976) has documented the presence of multiple populations of plagioclase primocrysts in the lower part of the drill core, with a correspondingly large compositional spread (e.g. Fig. 11). A complete study of the record of multiple magma injections preserved in the plagioclase of the cumulates would necessitate a detailed and quantitative study of major and trace elements in the different types of plagioclase cores, building on the work of Maaløe (1976).

The presence of multiple, distinct, olivine populations in several samples in the lower part of the core (Fig. 11) suggests that the early inflation of the magma chamber involved many different small batches of olivine-phyric magma. That the incoming magma batches may also have been plagioclase-phyric is suggested by the abundance of complex resorbed plagioclase cores between –150 and –100 m stratigraphic height that could be indicative of mixing of different phenocryst loads. The presence of the complex plagioclase cores in cumulates up to 30 m stratigraphic height (Maaløe, 1976) may indicate that the cumulates up to this point contain mixed populations of plagioclase primocrysts. It is interesting that, although no details were given, a mixed population of plagioclase primocrysts is present throughout most of the HZ (Maaløe, 1976), whereas polymodal olivine populations are present only at certain stratigraphic horizons (Fig. 11). This difference may be linked to the ease with which plagioclase may be suspended in a convecting magma and the difficulty of diffusional resetting of compositional zoning in plagioclase, resulting in the scattering of compositionally distinct plagioclase from any influx of magma through a significant stratigraphic thickness. In contrast, the higher density of olivine and the relatively rapid diffusional resetting of compositional differences means that polymodal olivine populations are likely to be concentrated in the horizon representative of the magma–mush interface at the moment the incoming magma arrived in the chamber.

The upper part of the core differs significantly from the lower, with a relatively constant Mg-number, the absence of resorbed plagioclase cores (Maaløe, 1976), and a gradual increase of bulk-rock concentrations of V with stratigraphic height (Fig. 10; suggestive of control by closed-system fractionation). These features suggest that the cumulates of the upper part of the core are likely to have formed in a closed system. The major geochemical and microstructural discontinuity in the region of –8·8 to –2·5 m is therefore consistent with this part of the intrusion recording the last magma influx that inflated the chamber to its final size, signalling the closure of the fractionating system. It should be noted, however, that this region of the core does not contain samples with polymodal olivine, suggesting either that any such magma did not contain significant numbers of olivine phenocrysts, or that any such phenocrysts did not survive to become part of the cumulate stratigraphy or were modified beyond the possibility of recognition.

Progressive inflation of the Skaergaard magma chamber

The geochemical and microstructural data for the lower part of the core potentially provide us with information about the timing, composition and size of the multiple batches of magma that contributed to the early stages of inflation of the Skaergaard chamber. The kinds of features expected to record episodes of chamber filling are observed in several places in the drill core. As described in detail below, these are the region between –120 and –100 m, the olivine-rich layers at –89 and –65 m, and the region immediately overlying the –8·8 m olivine-rich layer.

Holness *et al.* (2007*a*) interpreted the low dihedral angles at the base of the drill core to be indicative of a quench zone. However, the gabbros in the lowermost 25 m of the drill core are coarse-grained, retain a recognizably primary igneous microstructure and have cumulate, rather than liquid, compositions—these rocks therefore cannot represent the chilled margin of a chamber of the size of the current intrusion. In unfractionated dolerites, relatively low angles of ~80° result from crystallization times shorter than ~10 years (Holness *et al.*, 2012*b*). Although values of Θ_{cpp} in layered intrusions are not directly comparable with those in (essentially unfractionated) sills (Holness *et al.*, 2013*a*) the low Θ_{cpp} at the base of the drill core is most probably caused by relatively rapid crystallization. We suggest that the lowermost part of the drill core crystallized from a small sill-like injection of basaltic magma that formed at the contact between the Precambrian gneiss and the overlying sequence of plateau lavas. Well before it crystallized fully, this initial intrusion was inflated by the arrival of successive magma batches to become the Skaergaard magma chamber. The low bulk-rock Mg-number, and an olivine primocryst composition of $Fo_{55–60}$, suggests that this initial magma batch was relatively evolved. The sparse preliminary data suggest that clinopyroxene in these lowermost rocks may have a particularly low Cr content (Fig. 13), consistent with crystallization from an evolved liquid. The proportion of augite is relatively high (Fig. 14), with some of the samples from the base of the core lying outside the triangle formed by liquid, plagioclase and olivine (Fig. 15) perhaps indicative of cumulus status, although there is nothing in the morphology to substantiate this (see discussion below).

From –124 m, the bulk-rock Mg-number and the forsterite content of the olivine increase significantly over a stratigraphic distance of ~20 m (Figs 6 and 11). Three samples in this region contain polymodal olivine populations (at –119·5, –117·3 and –108·8 m, Fig. 11) and Θ_{cpp} increases locally to form a significant peak between –117·3 and –108·8 m (Fig. 6). There is no layering or change in the mineral mode in this part of the core, which is generally rather featureless and uniform. The changes in bulk-rock Mg-number and olivine composition, and the samples with polymodal olivine populations, suggest that the core is recording the arrival of at

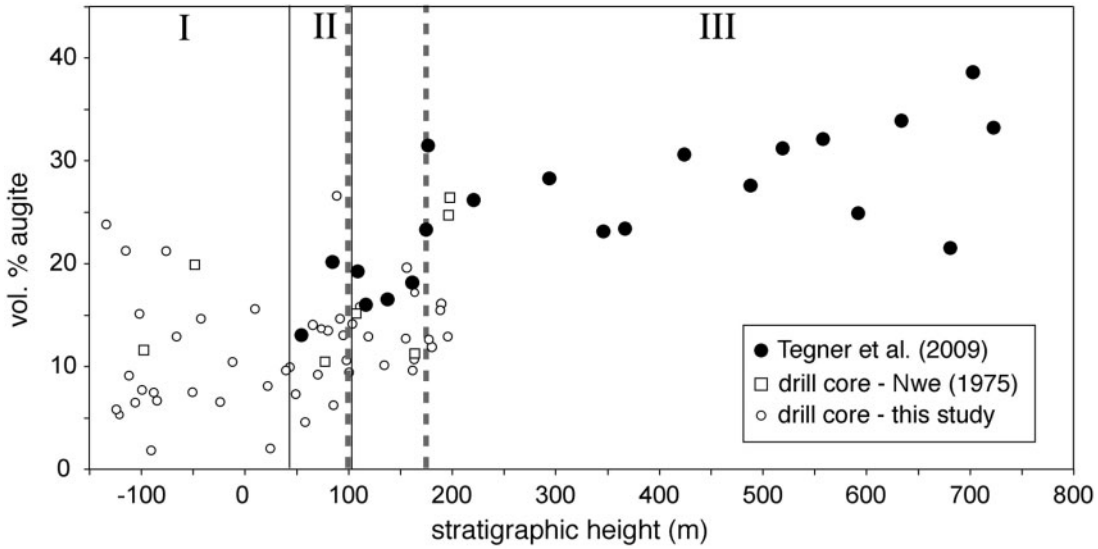

Fig. 14. The volumetric fraction of augite through the core as a function of stratigraphic height [data from this study and from Nwe (1975)], compared with that in the Tegner *et al* (2009) reference profile through the lower part of the Layered Series (re-measured as part of this study). The two vertical dashed lines show the position of the stepwise increase in Θ_{cpp} at 100 m and the position of the LZa–b boundary in the Tegner *et al.* (2009) sample set. The two continuous lines show the three subdivisions of Nwe (1975, 1976) relating to her inferences regarding the cumulus status of augite.

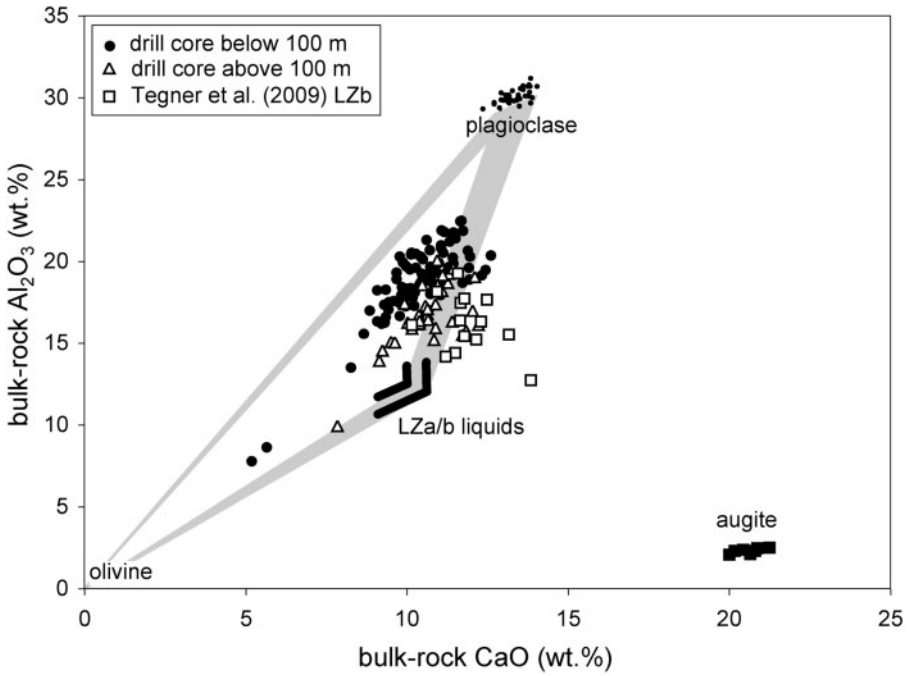

Fig. 15. The variation of bulk-rock Al_2O_3 with bulk-rock CaO for the drill core samples, differentiated according to whether the samples lie above or below 100 m stratigraphic height. For comparison the samples allocated to LZb by Tegner *et al.* (2009) are also plotted. The plagioclase and augite compositions plotted were obtained as part of this study. The two liquid trajectories (shown as bold black lines) are taken from Thy *et al.* (2009) and Tegner & Cawthorn (2010).

least three separate batches of relatively primitive, hot, olivine-phyric magma between –124 and –117 m stratigraphic height. The absence of any modal changes is consistent with these batches of incoming magma mixing with the resident magma in the progressively inflating chamber, as expected for a relatively buoyant liquid. Although there is no reduction in grain size, demonstrating that the incoming magma was not chilled sufficiently to trigger a very high nucleation rate, the increase of both P_2O_5 and K_2O at –124 m (Fig. 9) points to a higher than usual amount of trapped liquid, consistent with relatively rapid crystallization immediately following magma injection. The positive excursion in Θ_{cpp} occurs slightly higher, at –117 m: it may be a

consequence of increased crystallization times (e.g. Holness *et al.*, 2012*a*, 2012*b*) caused by the pulse of hot incoming magma.

The horizon at about –89 m is marked by an abrupt decrease between –86·6 and –85·4 m in bulk-rock Mg-number. Olivine compositions show a marked decrease in forsterite content (Fig. 11). There is no significant change in either Θ_{cpp} or grain size. These observations are consistent with the arrival of a batch of relatively evolved, cool and dense liquid. We speculate that the gradual increase in Mg-number upwards from the −89 m olivine-rich layer documents the progressive mixing of the ponded magma on the chamber floor with the overlying, more primitive, bulk magma.

The olivine-rich layer at –65 m is associated with locally forsterite-rich olivine (Fig. 11) and a localized increase of bulk-rock Mg-number (Fig. 6), consistent with the arrival of relatively primitive magma. The highly localized nature of these compositional excursions and the absence of a well-constrained change in Θ_{cpp} suggest that this influx was quickly and thoroughly mixed with the resident magma.

The region of the core between –24 m and about 40 m stratigraphic height records major changes of Θ_{cpp}, grain size, modal mineralogy and trace element composition. This region is therefore likely to be the most significant part of the core in terms of the chamber filling history.

The geochemical and microstructural changes in this region of the core are not exactly stratigraphically coincident. The stratigraphically lowest recorded 'event' is the extreme enrichment in P_2O_5 and K_2O at –24 m (typified by sample 722′8″, Table 2, Fig. 9). At –8·8 m we see the base of a thin fine-grained olivine-rich layer that is marked by an abrupt decrease in grain size (Fig. 5), a reduction in incompatible element concentrations (Figs 9 and 10) and two samples with relatively forsterite-rich olivine (–8·6 and –5·5 m, Fig. 11). Θ_{cpp} increases in a stepwise fashion at –2·5 m and decreases upwards through the stratigraphy towards background values over ∼12 m (Fig. 5).

That the region of the core between –24 and 40 m records the arrival of a substantial volume of magma, and the inflation of the Skaergaard chamber to its final size, is suggested by the generally smoothly increasing CaO/Al_2O_3, V and Y concentrations, relatively smoothly decreasing Fo and An contents of olivine and plagioclase respectively (although see subsequent discussion of the smaller-scale olivine compositional variation in the region 0–30 m), and the absence of wide variation in bulk-rock Mg-number, K_2O concentration and Θ_{cpp} (excepting the step-change in Θ_{cpp} at 100 m) in the upper half of the core. These features indicate a well-mixed, closed and homogeneous, magma body, subject to a thermal history dictated entirely by its own enthalpy budget.

The olivine-rich layer at –8·8 m, with its abrupt decrease in grain size, is reminiscent of the intra-plutonic quench zones in the Kap Edvard Holm intrusion, associated with magma influx (Tegner *et al.*, 1993). However, it is not clear that the grain-size reduction in the Skaergaard drill core represents a chill; instead of occurring at the same horizon as the increase in Θ_{cpp}, as seen at Kap Edvard Holm (Holness *et al.*, 2012*a*), it underlies it by 6 m (Fig. 5). Furthermore, the fine-grained rocks at –8·6 m and above contain low concentrations of incompatible elements, signifying small volumes of trapped liquid, whereas the bulk composition of the Kap Edvard Holm quench zones is close to that of likely replenishing magmas (Tegner *et al.*, 1993). Instead, it is possible that the olivine-rich layer formed either as a consequence of abundant nucleation and accumulation of olivine, perhaps in non-cotectic proportions and triggered by pressure changes associated with the arrival of a large volume of magma in a fault-bounded chamber (see Nielsen, 2004), or as an accumulation of crystals brought in by the new magma. It is intriguing that the olivine-rich layer closely overlies a highly incompatible element rich zone, and it is tempting to speculate that rapid accumulation of an impermeable cap of olivine may have resulted in the trapping of abundant evolved liquid in the underlying crystal mush.

The broad peak in Θ_{cpp} and the presence of relatively forsterite-rich olivine at –8·6 and –5·5 m suggests not only that the incoming magma was hot and primitive, resulting in a reduced cooling rate of the chamber as a whole, but also that the incoming magma may have been olivine-phyric. That relatively forsterite-rich olivine is seen in only two samples may be a consequence of rapid and efficient mixing of the relatively buoyant incoming magma with that resident in the chamber, with little opportunity to develop either a geochemically distinct ponded layer on the chamber floor or a distinct layer of entrained grains of forsterite-rich olivine.

The interval between –2·5 m and about 50 m is marked by a thick felsic layer, together with a zone of fairly well-defined modal layering. Holness *et al.* (2007*a*) suggested that a major overturn of the chamber occurred here. The zone of modal layering might therefore mark the onset of vigorous convection and mixing in the newly enlarged chamber. The olivine in the region 0–30 m stratigraphic height (i.e. in the feldspar-rich horizon) shows a steadily and sharply decreasing forsterite content, followed by an increase at about 45 m (Fig. 11). Although the reduction could be taken as support for fractionation of a small body of magma, there is no field evidence for the presence of such a body in the lower parts of the exposed stratigraphy. The fluctuations in olivine composition might be a consequence of incomplete and continuing mixing of the bulk magma in the newly inflated chamber.

THE ARRIVAL OF CUMULUS AUGITE

The boundary between LZa and LZb was defined by Wager & Deer (1939) as the horizon at which augite becomes cumulus, characterized by a change in pyroxene morphology from poikilitic to a more equidimensional

habit (McBirney, 1989*b*). McBirney (1989*b*) noted that occasional rocks with poikilitic pyroxene are found above the nominal boundary, but that it is mappable and regular on the scale of the intrusion.

Tegner *et al.* (2009) placed the LZa–b boundary at 175 m stratigraphic height (Fig. 14) in a suite of surface samples collected 1 km north of the drill core, associated with a significant increase in augite mode. Nwe (1975) found a high augite mode in samples above 196 m stratigraphic height in the Cambridge Drill Core (Table 3), but argued that a gradual change in augite morphology, from poikilitic (zone I, Fig. 6) to granular (zone III, Fig. 6), suggests that augite is a cumulus phase above ~100 m stratigraphic height. Further evidence that might support Nwe's suggestion that augite is cumulus above 100 m in the drill core is provided by the presence of weak modal layering defined by slight variations in augite mode above this height (Maaløe, 1987). The stepwise increase of Θ_{cpp} described by Holness *et al.* (2007*a*) (Fig. 6) occurs at 100 m in the drill core and, although the spacing of the surface samples described by Tegner *et al.* (2009) is relatively large, the step occurs between 84 and 96 m stratigraphic height in the Tegner *et al.* sample suite (Holness *et al.*, 2007*a*). As argued above, the stepwise increase in Θ_{cpp} marks the base of the mushy layer at the moment the bulk magma became saturated in augite, so the actual stratigraphic position at which augite becomes cumulus must lie higher than this. The close sample spacing permitted with the drill core allows a detailed investigation of the behaviour of augite as a case study of the arrival of a new cumulus phase.

Augite trace element concentrations

According to the classical paradigm for cumulate formation [as originally set out by Wager *et al.* (1960)] if augite and oxides are both intercumulus their Cr content must be determined by the composition of the interstitial liquid. In the early stages of fractionation, when neither augite nor oxides are cumulus phases, continued fractionation results in the remaining bulk magma (and thus the starting composition of the interstitial liquid in the mush on the magma chamber floor) becoming progressively richer in Cr. Accordingly, the interstitial augite should also become richer in Cr upwards through the stratigraphy. Once the bulk magma is saturated in augite, the Cr content of cumulus augite should begin to decrease with stratigraphic height, as the Cr is preferentially partitioned into the cumulus grains. The highest Cr contents should be observed in the cumulus cores, whereas the rims, formed by growth within the mush from the interstitial liquid, should have lower Cr.

The observed Cr contents in augite from the drill core and exposed parts of the Layered Series do not follow the expected pattern (Fig. 13b). Instead, following a major increase in Cr content between –85 and –24 m (probably related to the magma influxes described in the previous section) we see a progressive decrease of Cr in augite through LZa and into LZb. Although our conclusions are limited by the few samples studied in this preliminary investigation (and in particular by the large gap between the bulk of the analyses and the stratigraphically highest sample analysed), there is no obvious clear step-change in the rate of decrease associated with the samples above 100 m stratigraphic height. The trace element composition of augite does not offer a clear answer to the stratigraphic position of the arrival of cumulus augite (although it would be instructive to undertake more analyses through LZb from the exposed stratigraphy).

Bulk-rock composition

Modal layering defined by variations in the augite mode (e.g. Maaløe, 1987) is manifest by highly variable bulk-rock Cr content in Nwe's zone III (Fig. 6). Furthermore, Nwe's zone II is characterized by a smooth and steady increase in bulk Cr content from ~60 to ~180 ppm, consistent with both an increased augite mode and an increasing influence of the bulk magma on the composition of the interstitial augite (i.e. it is increasingly growing from liquid in the upper part of the mushy layer rather than from interstitial liquid deep in the mush). The relative influence of these two factors on bulk-rock Cr content is not clear. If the three-fold increase of bulk-rock Cr in Nwe's zone II is entirely due to an increased mode we would expect to see a tripling of the augite mode in this interval; this is not seen in the region of 100–175 m (Fig. 14). Given the number of thin sections analysed for mineral modes, we doubt the consistent absence of high augite modes is a consequence of inaccuracies in our determinations of modal proportion. We suggest instead that the increase in Cr may be caused by an increasing influence of the bulk magma composition on augite growing within the mush.

The ratio of CaO to Al_2O_3 in the bulk-rock composition should provide an indication of whether augite is a cumulus phase. The stratigraphic variation of the CaO/Al_2O_3 ratio correlates strongly with bulk-rock Cr content (Fig. 6), with the same steady and smooth increase through Nwe's zone II into a highly variable zone III. On a plot of bulk CaO vs Al_2O_3, a troctolitic cumulate should plot within the triangular region defined by the average olivine and plagioclase compositions and the average composition of the bulk liquid. A gabbroic cumulate should plot outside this triangle, towards the composition typical of cumulus augite. Almost all our drill core data below 100 m stratigraphic height plot inside the triangle (Fig. 15), apart from some data from the base of the core. Many samples from above 100 m plot inside the triangle although the population is significantly displaced towards augite. Almost all the samples from the Tegner reference profile that were assigned to LZb by Tegner *et al.* (2009) plot outside the triangle, consistent with the presence of cumulus augite.

The displacement towards augite of samples from above 100 m stratigraphic height in the drill core could be explained by a significantly greater component of interstitial liquid in these rocks, but the absence of a corresponding increase in the concentration of P_2O_5, TiO_2 or K_2O (Fig. 9) demonstrates that highly evolved interstitial liquid was not retained. We suggest instead that the drill core above 100 m is slightly enriched in augite relative to plagioclase and olivine, consistent with higher bulk-rock Cr. However, this higher augite mode is lower than that expected for a gabbroic cumulate.

Augite morphology

The compactness changes very smoothly through the drill core (Fig. 7c) and, despite clearly granular augite at the top of the core (and hence a cumulus status at this point), the data do not provide a clearly defined division between poikilitic and granular habit that could be used to locate the arrival of augite as a cumulus phase. However, we suggest that the locally high values of n/A (Fig. 7a) and domain size (Fig. 7b) above 100 m are consistent with augite grains beginning to nucleate in large numbers above this level. This is suggestive of either cumulus status or a highly porous mushy layer in which the interstitial liquid was in chemical communication with the overlying bulk magma.

In summary, the Cr concentrations, the CaO/Al_2O_3 ratio and augite morphology all show noticeable changes above 100 m, although the cumulates do not contain the amount of augite expected for gabbroic cumulates until 196 m. There is insufficient evidence for a confident determination of the stratigraphic height in the drill core at which augite joins the cumulus assemblage.

CONCLUSIONS

The record of the early history of the Skaergaard magma chamber involves the arrival of many small batches of magma, each with a variable load of olivine and plagioclase phenocrysts. The region of the core between –120 and –108·8 m records at least three separate but closely spaced influxes, with more magma arriving at times marked by the horizons at –85 and –65 m stratigraphic height. The last influx of magma is recorded by the cumulates just below the lowest exposed horizons of the Layered Series, involving a large volume of magma that inflated the chamber to its final size. The earliest history of the Skaergaard magma chamber therefore involves the progressive inflation of a small, most probably tabular, body of relatively evolved magma, likely to have been a sill, situated at the discontinuity between the Precambrian gneisses and the overlying plateau lavas, by the addition of many separate magma batches. The arrival of discrete variably fractionated magma batches is recorded in polymodal olivine populations, chemically distinct populations of plagioclase (Maaløe, 1976), changes in bulk-rock composition and in the microstructure. The actual number of magma batches may have been higher, as a record is left only if the composition, temperature and crystal load of the incoming magma differs sufficiently from the resident magma. The 'Skaergaard parental magma' should therefore be viewed as the integrated and mixed composition of the various batches of magma that combined to inflate the chamber to its final size.

The stratigraphic position at which augite becomes cumulus is not clearly defined in the drill core on either the morphological or chemical grounds we investigated. Further work is required to find more robust ways of demonstrating bulk magma saturation in augite.

ACKNOWLEDGEMENTS

L.P.'s contribution to this study was part of his final undergraduate year at Cambridge University and the support of Trinity College, Cambridge, is gratefully acknowledged. L.P. thanks Graham Smith for advice and help in textural analysis. We are grateful to Michael Higgins, Brian O'Driscoll, Jean-Clair Duchesne and Marjorie Wilson for helpful and constructive comments that significantly improved the paper.

FUNDING

C.T. and M.B.H. were supported by a Royal Society International Joint Project grant, and by the Carlsberg Foundation. C.T. was also supported by the Danish Council of Independent Research and the Danish National Research Foundation. The project was supported by the Natural Environment Research Council (grant number NE/F020325/1). O.N. acknowledges support from Magdalene College (University of Cambridge) and the von Humboldt Foundation (Germany; University of Hannover).

SUPPLEMENTARY DATA

Supplementary data for this paper are available at *Journal of Petrology* online.

REFERENCES

Annen, C., Pichavant, M., Bachmann, O. & Burgisser, A. (2008). Conditions for the growth of a long-lived shallow crustal magma chamber below Mount Pelee volcano (Martinique, Lesser Antilles Arc). *Journal of Geophysical Research* **113**(**B07209**), doi:10.1029/2007JB005049.

Annen, C., Paulatto, M., Sparks, R. S. J., Minshull, T. A. & Kiddle, E. J. (2014). Quantification of the intrusive magma fluxes during magma chamber growth at Soufrière Hills Volcano (Montserrat, Lesser Antilles). *Journal of Petrology* **55**, 529–548.

Armstrong, J. T. (1995). Citzaf: a package for correction programs for the quantitative electron beam X-ray analysis of thick polished materials, thin-films, and particles. *Microbeam Analysis* **4**, 177–200.

Ballhaus, C. G. & Glikson, A. Y. (1989). Magma mixing and intraplutonic quenching in the Wingellina Hills intrusions, Giles Complex, Central Australia. *Journal of Petrology* **30**, 1443–1469.

Barnes, S. J. (1986). The effect of trapped liquid crystallisation on cumulus mineral compositions in layered intrusions. *Contributions to Mineralogy and Petrology* **93**, 524–531.

Brooks, C. K. & Nielsen, T. F. D. (1978). Early stages in the differentiation of the Skaergaard magma as revealed by a closely related suite of dike rocks. *Lithos* **11**, 1–14.

Campbell, I. H. & Turner, J. S. (1989). Fountains in magma chambers. *Journal of Petrology* **30**, 885–923.

Class, C. & Goldstein, S. L. (1997). Plume–lithosphere interactions in the ocean basins: constraints from the source mineralogy. *Earth and Planetary Science Letters* **150**, 245–260.

Clemens, J. D. & Mawer, C. K. (1992). Granitic magma transport by fracture propagation. *Tectonophysics* **204**, 339–360.

de Saint-Blanquat, M., Habert, G., Horsman, E., Morgan, S. S., Tikoff, B., Launeau, P. & Gleizes, G. (2006). Mechanisms and duration of non-tectonically assisted magma emplacement in the upper crust: The Black Mesa pluton, Henry Mountains, Utah. *Tectonophysics* **428**, 1–31.

Eales, H. V. & Cawthorn, R. G. (1996). The Bushveld Complex. In: Cawthorn, R. G. (ed.) *Layered Intrusions. Developments in Petrology* **15**, 181–230.

Govindaraju, K. (1994). Compilation of working values and sample description for 383 geostandards. *Geostandards and Geoanalytical Research* **18**, 1–158.

Govindaraju, K. (1995). Working values with confidence limits for twenty-six CRPG, ANRT and IWG-GIT geostandards. *Geostandards and Geoanalytical Research* **19**, 1–32.

Griffin, W. L., Powell, W. J., Pearson, N. J. & O'Reilly, S. Y. (2008). Glitter: data reduction software for laser ablation ICP-MS. In: Sylvester, P. (ed.) *Laser Ablation ICP-MS in Earth Sciences. Mineralogical Association of Canada, Short Course* **40**, 204–207.

Grocott, J., Arevalo, C., Welkner, D. & Cruden, A. (2009). Fault-assisted vertical pluton growth: Coastal Cordillera, north Chilean Andes. *Journal of the Geological Society, London* **166**, 295–301.

Henderson, P. (1975). Geochemical indicator of the efficiency of fractionation of the Skaergaard intrusion, East Greenland. *Mineralogical Magazine* **40**, 285–291.

Higgins, M. D. (1994). Numerical modelling of crystal shapes in thin sections: estimation of crystal habit and true size. *American Mineralogist* **79**, 113–119.

Higgins, M. D. (2000). Measurement of crystal size distribution. *American Mineralogist* **85**, 1105–1116.

Holness, M. B. & Winpenny, B. (2009). The Unit 12 allivalite, Eastern Layered Intrusion, Isle of Rum: a textural and geochemical study of an open-system magma chamber. *Geological Magazine* **146**, 437–450.

Holness, M. B., Nielsen, T. F. D. & Tegner, C. (2007a). Textural maturity of cumulates: a record of chamber filling, liquidus assemblage, cooling rate and large-scale convection in mafic layered intrusions. *Journal of Petrology* **48**, 141–157.

Holness, M. B., Tegner, C., Nielsen, T. F. D., Stripp, G. & Morse, S. A. (2007b). A textural record of solidification and cooling in the Skaergaard intrusion, East Greenland. *Journal of Petrology* **48**, 2359–2377.

Holness, M. B., Humphreys, M. C. S., Sides, R., Helz, R. T. & Tegner, C. (2012a). Towards an understanding of disequilibrium dihedral angles in mafic rocks. *Journal of Geophysical Research* doi:10.1029/2011JB008902.

Holness, M. B., Richardson, C. & Helz, R. T. (2012b). Disequilibrium dihedral angles in dolerite sills: a new proxy for cooling rate. *Geology* **40**, 795–798.

Holness, M. B., Namur, O. & Cawthorn, R. G. (2013a). Disequilibrium dihedral angles in layered intrusions: a microstructural record of fractionation. *Journal of Petrology* **54**, 2067–2093.

Holness, M. B., Richardson, C. & Andersen, J. C. Ø. (2013b). The campsite dykes: a window into the early post-solidification history of the Skaergaard Intrusion, East Greenland. *Lithos* **182–183**, 134–149.

Hoover, J. D. (1989). Petrology of the Marginal Border Series of the Skaergaard Intrusion. *Journal of Petrology* **30**, 399–439.

Horn, I., Hinton, R. W., Jackson, S. E. & Longerich, H. P. (1997). Ultra-trace element analysis of NIST SRM 616 and 614 using laser ablation microprobe-inductively coupled plasma-mass spectrometry (LAM-ICP-MS): a comparison with secondary ion mass spectrometry (SIMS). *Geostandards and Geoanalytical Research* **21**, 191–203.

Humphreys, M. C. S. (2009). Chemical evolution of intercumulus liquid, as recorded in plagioclase overgrowth rims from the Skaergaard Intrusion. *Journal of Petrology* **50**, 127–145.

Huppert, H. E. & Sparks, R. S. (1980). The fluid dynamics of a basaltic magma chamber, replenished by hot, dense, ultrabasic magma. *Contributions to Mineralogy and Petrology* **75**, 279–289.

Irvine, T. N., Andersen, J. C. Ø. & Brooks, C. K. (1998). Included blocks (and blocks within blocks) in the Skaergaard intrusion: geological relations and the origins of rhythmic modally graded layers. *Geological Society of America Bulletin* **110**, 1398–1447.

Jakobsen, J. K., Tegner, C., Brooks, C. K., Kent, A. J. R., Lesher, C. E., Nielsen, T. F. D. & Widenbeck, W. (2010). Parental magma of the Skaergaard intrusion: constraints from melt inclusions in primitive troctolite blocks and FG-1 dykes. *Contributions to Mineralogy and Petrology* **159**, 61–79.

Jochum, K. P., Pfander, J., Woodhead, J. D., Willbold, M., Stoll, B., Herwig, K., Amini, M., Abouchami, W. & Hofmann, A. W. (2005). MPI-DING glasses: new geological reference materials for *in situ* Pb isotope analysis. *Geochemistry, Geophysics, Geosystems* **6**, Q10008, doi:10.1029/2005GC00995.

Jochum, K. P., Stoll, B., Herwig, K., et al. (2006). MPI-DING reference glasses for *in situ* microanalysis: New reference values for element concentrations and isotope ratios. *Geochemistry, Geophysics, Geosystems* **7**, Q02008, doi:10.1029/2005GC0011060.

Leuthold, J., Blundy, J. D., Holness, M. B. & Sides, R. (2014). Successive episodes of reactive liquid flow through a layered intrusion (Unit 9, Rum Eastern Layered Intrusion, Scotland). *Contributions to Mineralogy and Petrology* **167**, 1021, doi:10.1007/s00410-014-1021-7.

Maaløe, S. (1976). The zoned plagioclase of the Skaergaard Intrusion, East Greenland. *Journal of Petrology* **17**, 398–419.

Maaløe, S. (1978). The origin of rhythmic layering. *Mineralogical Magazine* **42**, 337–345.

Maaløe, S. (1987). Rhythmic layering of the Skaergaard Intrusion. In: Parsons, I. (ed.) *Origins of Igneous Layering*. Dordrecht: D. Riedel, pp. 247–262.

McBirney, A. R. (1989a). *Geological map of the Skaergaard Intrusion, East Greenland, 1:20 000*. Eugene, OR: Department of Geology, University of Oregon.

McBirney, A. R. (1989b). The Skaergaard Layered Series: I. Structure and average compositions. *Journal of Petrology* **30**, 363–397.

McBirney, A. R. (1996). The Skaergaard intrusion. In: Cawthorn, R. G. (ed.) *Layered Intrusions. Developments in Petrology* **15**, 147–180.

Menand, T. (2008). The mechanics and dynamics of sills in layered elastic rocks and their implications for the growth of laccoliths and other igneous complexes. *Earth and Planetary Science Letters* **267**, 93–99.

Michel, J., Baumgartner, L., Putlitz, B., Schaltegger, U. & Ovtcharova, M. (2008). Incremental growth of the

Patagonian Torres del Paine laccolith over 90 k.y. *Geology* **36**, 459–462.

Namur, O., Charlier, B., Toplis, M. J., Higgins, M. D., Liégeois, J.-P. & Vander Auwera, J. (2010). Crystallization sequence and magma chamber processes in the ferrobasaltic Sept Iles layered intrusion, Canada. *Journal of Petrology* **51**, 1203–1236.

Namur, O., Charlier, B., Toplis, M. J., Higgins, M. D., Hounsell, V., Liégeois, J. P. & Vander Auwera, J. (2011). Differentiation of tholeiitic basalt to A-type granite in the Sept Iles layered intrusion, Canada. *Journal of Petrology* **52**, 487–539.

Namur, O., Humphreys, M. C. S. & Holness, M. B. (2014). Crystallization of interstitial liquid and latent heat buffering in solidifying gabbros: Skaergaard Intrusion, Greenland. *Journal of Petrology* **55**, 1389–1427.

Nielsen, T. F. D. (1978). The Tertiary dike swarms of the Kangerdlugssuaq area, East Greenland. *Contributions to Mineralogy and Petrology* **67**, 63–78.

Nielsen, T. F. D. (2004). The shape and volume of the Skaergaard Intrusion, East Greenland: implications for mass balance and bulk composition. *Journal of Petrology* **45**, 507–530.

Norman, M. D., Griffin, W. L., Pearson, N. J., Garcia, M. O. & O'Reilly, S. Y. (1998). Quantitative analysis of trace element abundances in glasses and minerals: a comparison of laser ablation inductively coupled plasma mass spectrometry, solution inductively coupled plasma mass spectrometry, proton microprobe and electron microprobe data. *Journal of Analytical Atomic Spectrometry* **13**, 477–482.

Nwe, Y. Y. (1975). Aspects of the mineralogy of the Skaergaard intrusion, East Greenland. PhD thesis, University of Cambridge.

Nwe, Y. Y. (1976). Electron-probe studies of the earlier pyroxenes and olivines from the Skaergaard Intrusion, East Greenland. *Contributions to Mineralogy and Petrology* **55**, 105–126.

Pearce, N. J. G., Perkins, W. T., Westgate, J. A., Gorton, M. P., Jackson, S. E., Neal, C. R. & Chenery, S. P. (1997). A compilation of new and published major and trace element data for NIST SRM 610 and MIST SRM 612 glass reference materials. *Geostandards Newsletter* **21**, 115–144.

Raedeke, L. D. & McCallum, I. S. (1984). Investigations in the Stillwater Complex: Part II. Petrology and petrogenesis of the Ultramafic Series. *Journal of Petrology* **25**, 395–420.

Rasband, W. (2007). ImageJ. US National Institutes of Health, Bethseda, MD. http://rsb.info.nih.gov/ij/.

Renner, R. & Palacz, Z. (1987). Basaltic replenishment of the Rhum magma chamber: evidence from Unit 14. *Journal of the Geological Society, London* **144**, 961–970.

Royet, J. P. (1991). Stereology: a method for analysing images. *Progress in Neurobiology* **37**, 433–474.

Salmonsen, L. P. & Tegner, C. (2013). Crystallisation sequence of the Upper Border Series of the Skaergaard Intrusion: revised subdivision and implications for chamber-scale magma homogeneity. *Contributions to Mineralogy and Petrology* **165**, 1155–1171.

Stickels, C. A. & Hücke, E. E. (1964). Measurement of dihedral angles. *Transactions of the Metallurgical Society of the AIME* **230**, 795–801.

Tegner, C. & Cawthorn, R. G. (2010). Iron in plagioclase in the Bushveld and Skaergaard intrusions: implications for iron contents in evolving basic magmas. *Contributions to Mineralogy and Petrology* **159**, 719–730.

Tegner, C., Wilson, J. R. & Brooks, C. K. (1993). Intraplutonic quench zones in the Kap Edvard Holm layered gabbro complex, East Greenland. *Journal of Petrology* **34**, 681–712.

Tegner, C., Thy, P., Holness, M. B., Jakobsen, J. K. & Lesher, C. E. (2009). Differentiation and compaction in the Skaergaard intrusion. *Journal of Petrology* **50**, 813–840.

Thomsen, V. (2007). Basic fundamental parameters in X-ray fluorescence. *Spectroscopy* **22**, 46–50.

Thy, P., Lesher, C. E. & Tegner, C. (2009). The Skaergaard liquid line of descent revisited. *Contributions to Mineralogy and Petrology* **157**, 735–747.

Van Sprang, H. A. (2000). Fundamental parameter methods in XRF spectroscopy. *Advances in X-ray Analysis* **42**, 1–10.

VanTongeren, J. A., Mathez, E. A. & Kelemen, P. B. (2010). A felsic end to the Bushveld differentiation. *Journal of Petrology* **51**, 1891–1912.

Wager, L. R. (1960). Major and trace element variation of the Layered Series of the Skaergaard Intrusion and a re-estimate of the average composition of the Hidden Layered Series and of the successive residual magmas. *Journal of Petrology* **1**, 364–398.

Wager, L. R. & Brown, G. M. (1968). *Layered Igneous Rocks*. San Francisco, CA: Freeman.

Wager, L. R. & Deer, W. A. (1939). *Geological investigations in East Greenland.* Part III. The petrology of the Skaergaard intrusion, Kangerdlussuaq, East Greenland. *Meddelelser om Grønland* **105**(**4**).

Wager, L. R., Brown, G. M. & Wadsworth, W. J. (1960). Types of igneous cumulates. *Journal of Petrology* **1**, 73–85.

Wilson, A. H. (2012). A chill sequence to the Bushveld Complex: insight into the first stage of emplacement and implications for the parental magmas. *Journal of Petrology* **53**, 1123–1168.